



AIAA 2002-3891

**Rocket Gas Dynamics for an Arbitrary
Mean Flowfield**

Joseph Majdalani
Marquette University
Milwaukee, WI 53233

Propulsion Conference and Exhibit

7–10 July 2002

Indianapolis, IN

Rocket Gas Dynamics for an Arbitrary Mean Flowfield

Joseph Majdalani*

Marquette University, Milwaukee, WI 53233

and

Gary A. Flandro†

University of Tennessee Space Institute, Tullahoma, TN 37388

The linearized Navier-Stokes equations play a central role in describing the unsteady motion of a viscous fluid inside a porous tube. Asymptotic solutions of these equations have been found and here we extend the class of known solutions by solving the problem for an arbitrary mean flow function of the Berman type. In the process, we show how not only do we recover, confirm, or correct some of the previously known solutions, but also find some completely new forms. It is interesting that, for sufficiently small injection, the Sextl profile can be restored from ours. Furthermore, we find that analytical, numerical, and experimental results obtained by other investigators compare favorably with ours. The methods we apply provide accurate expressions for the main flow variables and help describe the ensuing oscillatory field. By appealing to a space-reductive multiple-scale technique, the problem's underlying length scale is rigorously derived. Our results indicate that, irrespective of the mean flow details, the unsteady component of vorticity initiated by small pressure disturbances can be more intense than its mean counterpart. No vortical study in porous tubes can therefore be complete unless it incorporates the unsteady field contribution.

I. Introduction

MUCH attention has been given to the description of internal flows established inside circular tubes with transpiring walls. Depending on whether fluid is being added or withdrawn, examples cited in the literature have ranged from paper making,¹ to the modeling of biological flows,² to simulations of the combustion-induced gas motion inside solid rocket motors.³ Research motivation was spurred on by a series of interesting technological processes. Pertinent applications have included flow filtration, isotope separation, surface ablation, pulmonary circulation, and arterial blood flow modeling. Whereas earlier studies have focused on steady laminar flow analyses, the more challenging temporal aspects have been deferred to later investigations. In order to gain perspective on the problem at hand, a brief summary will now be presented.

The earliest account of steady flow solutions in channels with porous boundaries can be attributed to

Berman.⁴ Provided that fluid was being injected or removed uniformly through the sidewalls, Berman was able to introduce a technique that reduced the Navier-Stokes system into a single ordinary differential equation. Following Berman's landmark paper, a number of studies appeared in succession. Most were often valid over restricted ranges of fluid injection or suction. Further studies addressed the issue of spatial development and stability along with the existence of unique or multiple solutions. Experimental investigations were reported as well.

For circular pipes and tubes, Yuan and Finkelstein⁵ presented asymptotic solutions in the limiting cases of small suction and both small and large injection. Their formulation depended on the crossflow Reynolds number R . This key parameter was based on the uniform injection speed V , tube radius a , and kinematic viscosity ν . For large R , their solution correctly reduced to the inviscid expression reported by Taylor,¹ that same year, for infinite injection.

After classifying each type of possible solutions based on the ranges of R , Terrill and Thomas⁶ attempted the method of inner and outer expansions to derive asymptotic solutions for each separate class. Contrary to the existing formulations of Yuan and Finkelstein,⁵ their approach indicated possible

*Assistant Professor, Department of Mechanical and Industrial Engineering. Member AIAA.

†Boling Chair Professor of Mechanical and Aerospace Engineering. Associate Fellow, AIAA.

multiplicity of solutions. It captured the viscous layer at the pipe centre and predicted two solutions for fixed injection rate. In later studies, Durlofsky and Brady⁷ would demonstrate the illegitimacy of one of their two solutions.

Since Terrill and Thomas⁶ could not distinguish between the two apparent types for the large suction case, Terrill⁸ invested further exploratory effort. He was able to show that inclusion of exponentially small terms in the method of asymptotic expansions could produce more accurate results. These corrective terms could serve to predict the range of values for which no solutions could be found numerically. A formal asymptotic analysis led by Skalak and Wang⁹ concurred with Terrill's predictions. Thus it was concluded that there existed at least two solutions for injection and, at most, four solutions for sufficiently large suction. In the process, elegant arguments were given regarding the necessary presence of multiple solutions for a given R . This issue was laid to rest following a rigorous mathematical treatment by Lu.¹⁰ In summary, it was found that two solutions for injection, one being unphysical, existed for all R . For suction, two solutions existed in the ranges $[0, 2.3]$ and $[9.1, 20.6]$, no solution existed in $[2.3, 9.1]$, and four solutions were possible when the suction Reynolds number exceeded 20.6. In this article, the only physical solution for injection will be of concern.

Using Berman's similarity transformation in a different physical setting, Brady and Acrivos¹¹ employed matched asymptotic expansions to treat the general problem of a tube with a linearly accelerating surface velocity. Inasmuch as the porous pipe flow problem could be reproduced from their generalized formulation, their results shared similar features to the foregoing predictions. The spatial stability of such self-similar flows was later addressed by Durlofsky and Brady.⁷ The physicality of corresponding similarity solutions was examined via small perturbations in the streamwise velocity. Taking into account the finite pipe length and the poor likelihood of an inlet velocity satisfying the similarity requirements, Brady¹² studied the spatial development of the velocity structure for arbitrary inlet profiles with suction or injection. He found that, when a critical suction Reynolds number was reached, the influence of inlet conditions extended throughout the tube. This behavior prevented the similarity solution from evolving and caused, instead, collision regions to form near the head end. No such patterns were found with injection.

The influence of both symmetric and asymmetric perturbations was investigated numerically, for the injection case, by Gol'dshtik and Ersh.¹³ Details showed that laminar solutions representing straight-through flow were stable for all injection. Conversely,

solutions containing an axial reverse-current zone were absolutely unstable, indicating the non-physicality of such solutions. For injection Reynolds numbers exceeding 100, their numerical solution agreed with the asymptotic formulation of Yuan and Finkelstein.⁵

Other flow properties, such as skin friction and heat transfer coefficients, have also been examined. The onset of turbulence is another issue that several investigators have attempted to characterize. For steady conditions, useful data can be gathered from Wageman and Guevara,¹⁴ Yuan and Brogren,¹⁵ Olson and Eckert,¹⁶ Sviridenkov and Yagodkin,¹⁷ Beddini,¹⁸ and Dunlap *et al.*¹⁹ The foregoing studies have confirmed the existence of a laminar segment whose size depended on the crossflow Reynolds number. They have also indicated that mean turbulent profiles differed only slightly from their laminar counterparts derived, for example, by Yuan and Finkelstein.⁵ Such studies reinforced the importance of laminar solutions.

The challenges of modeling flows inside porous tubes rises to a new level of complexity when oscillatory wave motion is superimposed. Such has been the case when cold-flow simulations were undertaken for the purpose of understanding the internal gas dynamics during solid propellant burning. A number of experimental studies have, in fact, attempted to capture the nature of velocity oscillations inside tubes with transpiring walls. Tests realized on reactive propellants have spanned a range of almost four decades. In order to both reduce the hazards of dealing with live propellants and, in an effort to facilitate data acquisition, alternative procedures were sought at times. The goal was to relay the inherent fluid dynamics while relying on safe simulations of the gas addition process. The answer was found, partly, in pursuing cold-flow simulations of the injection mechanism.

Several investigators have undertaken cold-flow experiments that use nitrogen, carbon dioxide, or air to simulate the injectant. By way of illustration, one can enumerate: Dunlap *et al.*,¹⁹ Ma, Van Moorhem and Shorthill,^{20,21} Barron, Majdalani and Van Moorhem,²² Griffond and Casalis,²³ and Casalis, Avalon and Pineau.²⁴ Most of these studies concentrated on reproducing an acoustic setting of the closed-closed boundary type. Such setting pertained to chambers that comprised impermeable head-end walls and choked flow at the downstream end. Acoustic closure at the aft end simulated rocket motors that (invariably) ended with a choked De Laval nozzle. Imposition of acoustic conditions of the closed-open type were also considered in cold-flow studies of nozzleless tubes. Being reserved to fewer applications, acoustic environments of the closed-open type received less attention. In the current study, formulations that apply to both acoustic types will be made available. However, the physical

description will focus on the closed-closed configuration.

Mathematical modeling of the oscillatory field over transpiring surfaces was chiefly developed by Culick³ and Flandro.²⁵⁻²⁸ In fact, the first analytical solution for the oscillatory field with infinitely large injection was successfully derived by Flandro.²⁶ This formulation was fictitiously two-dimensional: it ignored the downstream convection of unsteady vorticity and the radial depreciation of Taylor's mean flow profile. Consequently, it only applied to a small region above the porous wall and a restricted range of physical parameters. An asymptotic solution by Majdalani and Van Moorhem followed.^{29,30} The latter employed the exact Taylor profile yet shared its precursor's inability to incorporate the axial dependency.

Pursuant to Flandro's work, Zhao *et al.*³¹ resorted to multiple scales in order to analyze the developing transient flow that preceded the inception of steady-state oscillations. Zhao's approach provided a crude approximation since it was based on a conjectured set of scales found by intuition. Being the product of guesswork, these scales were different from the uniformly valid scales that were prescribed by the problem's solvability condition. As such, they differed from those derived by Majdalani³² and Majdalani and Roh.³³

An inviscid solution that incorporated the correct Taylor profile and axial dependency was later presented by Flandro.²⁷ This was quickly followed by an improved asymptotic solution that included viscous effects.²⁸ A practically equivalent solution was derived by Majdalani and Van Moorhem²⁹ using multiple-scale expansions. As shown by Majdalani and Van Moorhem,³⁴ both multidimensional solutions concurred with numerical simulations. They also showed fair agreement with data gathered from cold-flow experiments by Brown *et al.*³⁵ and Dunlap *et al.*¹⁹ Later, the multiple-scale solution was used to disclose the character of the Stokes boundary-layer structure in porous tubes.³⁶ Recently, the analogous problem arising in a planar channel has been addressed by Majdalani and Roh.³³

It should be pointed out that most existing analytical

solutions for the oscillatory field have been constructed by perturbing an initially steady mainstream that corresponds to the Taylor profile. As a result, they apply, in practice, to a very large influx through the peripheral walls. Such idealizations are quite suitable in simulating the relatively high rates of gas expulsion from propellant surfaces during solid rocket motor burning. In principle, they are limited to an infinitely large crossflow Reynolds number. On that account, it is the purpose of this article to generalize the techniques presented by Flandro,^{27,28} and Majdalani and Van Moorhem³⁴ by extending their applicability to arbitrary levels of injection. The resulting solutions should be useful over a broader range of physical applications. The article also serves as a vital extension to the planar solution presented recently by Majdalani and Roh.³³ Another novelty is that, whereas a partial WKB solution was presented before, a rigorous asymptotic treatment will be offered in Sec. IV leading to a complete WKB solution. In particular, the characteristic length scales that arise in the circular tube will now be derived using two space-reductive techniques in Secs. V and VI. While one appeals to Prandtl's principle of matching by supplementary expansions, the other will apply the principle of least singular behavior. For confirmation purposes, multiple independent verifications will be presented starting in Sec. VII with comparisons to other solutions. This is followed by a discussion in Sec. VIII wherein experimental and numerical verifications are provided based on the work carried out by Brown *et al.*³⁵ and Roh, Tseng and Yang.³⁷

II. Problem Formulation

A. The Finite Circular Tube

We consider the steady flow of a perfect gas in the region bounded by the porous walls of a cylindrical tube of radius a and finite length $L \gg a$. We assume that the speed of the gas at the wall V is uniform. We normalize spatial variables by a and select a curvilinear coordinate system whose origin is anchored at the tube's head-end centre. As shown in Fig. 1, x and r can be used to denote the non-dimensional

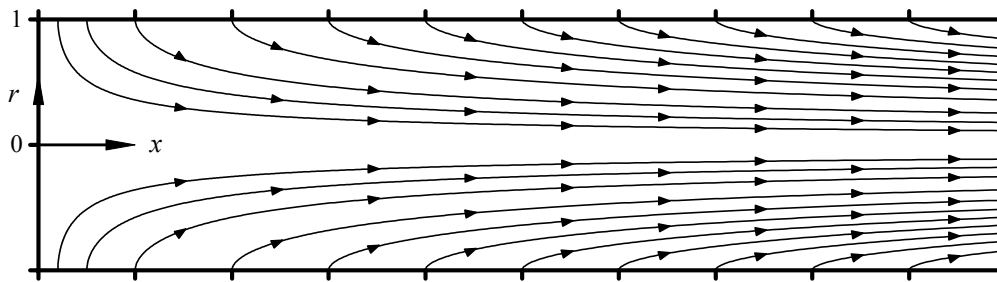


Fig. 1 Axisymmetric system geometry including mean flow streamlines.

streamwise and radial coordinates. Axial symmetry reduces the field investigation to the domain $0 \leq x \leq l$, and $0 \leq r \leq 1$, where $l = L/a < 70$. The tube is closed at $x=0$ corresponding to a zero inlet profile in Berman's formulation. As a result of this, the mainstream described by the streamline patterns of Fig. 1 is completely induced by the injection process. Inasmuch as we consider the case of choked flow at $x=l$ (where a nozzle can be located), we provide formulations that apply to an isobaric opening as well. The oscillatory field that we wish to evaluate will exist when the undisturbed state is perturbed via sinusoidal pressure oscillations of frequency ω and amplitude A . If c is the speed of sound, we follow Majdalani and Roh³³ by limiting our scope to low crossflow Mach numbers ($M = V/c < 0.01$) and small A by comparison to the mean stagnation pressure p_s .

B. Arbitrary Mean Flow Profile

Our point of departure is the self-similar mean flow solution in a tube with porous walls. Following Berman⁴ or Yuan and Finkelstein,⁵ we select a steady streamfunction Ψ that varies linearly in x . Without compromising generality, we employ $\Psi(x,r) = xF(r)$ and collapse the Navier–Stokes equations into

$$r^3 F'''' + r^2 R F'''' (F - 2\varepsilon) + R(F' - rF'') [rF' + 3(F - \varepsilon)] = 0; \quad \varepsilon \equiv 1/R. \quad (1)$$

In our notation, $R = Va/\nu > 0$ for injection. The mainstream velocity and vorticity vectors (normalized by V) can be expressed as $\mathbf{u}_0 = u_0 \mathbf{e}_x + v_0 \mathbf{e}_r$, and $\mathbf{\Omega}_0 = \Omega_0 \mathbf{e}_\theta$. Boundary conditions include the no-slip, $u_0(x,1) = 0$, radial influx at the wall, $v_0(x,1) = -1$, axial symmetry, $\partial u_0(x,0)/\partial r = 0$, and boundedness, $v_0(x,0) = 0$. From the streamfunction definition, one can write

$$u_0 = xF'/r, v_0 = -F/r, \Omega_0 = x(F'/r - F'')/r. \quad (2)$$

$$F'(1) = F(0) = 0, \lim_{r \rightarrow 0} (F'' - F'/r)/r = 0, F(1) = 1. \quad (3)$$

As discussed in Sec. I, a number of asymptotic solutions for F are available for different ranges of R (cf. Terrill and Thomas,⁶ or Terrill³⁸). From Yuan and Finkelstein,⁵ two simple solutions that are adequate for either small or large injection can be expressed as

$$F(r) = \begin{cases} r^2(2 - r^2) + O(10^{-2} R r^2), & 10 < R < 100 \\ \sin(\frac{1}{2} \pi r^2) + O(R^{-1}), & R > 100 \end{cases} \quad (4)$$

The mean pressure associated with Eq. (2) can be normalized by γp_s , where γ is the ratio of specific heats, and then integrated from the steady flow momentum equation, $\mathbf{u}_0 \cdot \nabla \mathbf{u}_0 = -M^{-2} \nabla p_0 + \varepsilon \nabla^2 \mathbf{u}_0$.

Recalling that $c = \sqrt{(\gamma p_s / \rho_s)}$ and that $p_0(0,0) = 1/\gamma$, one finds

$$p_0 = \frac{1}{\gamma} - \frac{1}{2} r^{-2} M^2 \left\{ F^2 + x^2 [F'^2 + (r^{-1} F' - F'')] \times (F - \varepsilon) - \varepsilon r F'''' \right\} + \varepsilon r F' = \gamma^{-1} + O(M^2 x^2) \quad (5)$$

Equation (5) concurs with the pressure distribution found by Yuan and Finkelstein,⁵ Wageman and Guevara,¹⁴ and Durlofsky and Brady.⁷ It indicates that the pressure variation in the axial direction is slow, justifying the usage of a constant value over the range $0 < x < 70$. It also explains the finite upper limit posted on the tube length in Sec. II.A.

C. Linearized Navier–Stokes Equations

In normalizing variables, the asterisk is used to designate dimensional quantities. The instantaneous velocity, pressure, density, spatial coordinates and time can be rendered dimensionless via

$$\mathbf{u} = \mathbf{u}^*/c, \quad p \equiv p^*/(\gamma p_s), \quad \rho \equiv \rho^*/\rho_s, \quad x = x^*/a, \quad r = r^*/a, \quad \text{and } t = t^*c/a. \quad (6)$$

With this choice of parameters, the Navier–Stokes equations with constant properties can be written as

$$\rho_t + \nabla \cdot (\rho \mathbf{u}) = 0, \quad (7)$$

$$\rho [\mathbf{u}_t + (\mathbf{u} \cdot \nabla) \mathbf{u}] = -\nabla p + \varepsilon M [4 \nabla (\nabla \cdot \mathbf{u}) / 3 - \nabla \times (\nabla \times \mathbf{u})]. \quad (8)$$

In the presence of small oscillations, the total pressure, density, and velocity can be expressed as linear sums of steady and temporal fluctuations:

$$p(x,r,t) = 1/\gamma + \bar{\varepsilon} p_1(x,r,t) + O(M^2), \quad (9)$$

$$\rho = 1 + \bar{\varepsilon} \rho_1, \quad \mathbf{u} = M \mathbf{u}_0 + \bar{\varepsilon} \mathbf{u}_1, \quad \mathbf{\Omega} = M \mathbf{\Omega}_0 + \bar{\varepsilon} \mathbf{\Omega}_1 \quad (10)$$

where $\bar{\varepsilon} = A/(\gamma p_s)$ is the wave amplitude ratio. When the expanded variables are inserted into Eqs. (7)–(8), two sets of equations are obtained at $O(1)$ and $O(\bar{\varepsilon})$. While the leading-order set reduces to Berman's nonlinear equation, the first-order set gives

$$(\rho_1)_t + \nabla \cdot \mathbf{u}_1 = -M \nabla \cdot (\rho_1 \mathbf{u}_0) + O(\bar{\varepsilon}), \quad (11)$$

$$(\mathbf{u}_1)_t = -M \left[\nabla (\mathbf{u}_0 \cdot \mathbf{u}_1) - \mathbf{u}_1 \times \mathbf{\Omega}_0 - \mathbf{u}_0 \times \mathbf{\Omega}_1 \right] - \nabla p_1 + \varepsilon M \left[4 \nabla (\nabla \cdot \mathbf{u}_1) / 3 - \nabla \times \mathbf{\Omega}_1 \right] + O(\bar{\varepsilon}). \quad (12)$$

In presetting the size of $\bar{\varepsilon}$, we adopt a notion used extensively in classic combustion stability theory, namely, that

$$M^2 < \bar{\varepsilon} < M, \quad \lim_{\bar{\varepsilon}, M \rightarrow 0} \frac{\bar{\varepsilon}}{M} = 0. \quad (13)$$

Accordingly, as we reduce M , $\bar{\varepsilon}$ will approach zero more rapidly.

D. Irrotational and Solenoidal Responses

Using the circumflex and tilde to designate irrotational and solenoidal responses (cf. Majdalani and Roh,³³) one may write

$$\mathbf{u}_1 = \hat{\mathbf{u}} + \tilde{\mathbf{u}}, \quad \text{with } \mathbf{\Omega}_1 = \tilde{\mathbf{\Omega}}, \quad p_1 = \hat{p}, \quad \rho_1 = \hat{\rho}. \quad (14)$$

Upon backward substitution into the linearized Navier–Stokes equations, one obtains two distinct sets. The first is the pressure-driven response which can be rearranged into

$$\begin{aligned} \hat{p}_t - \nabla^2 \hat{p} = & -M \left[\nabla \cdot (\mathbf{u}_0 \hat{p}_t) - \nabla^2 (\hat{\mathbf{u}} \cdot \mathbf{u}_0) \right. \\ & \left. + \nabla \cdot (\hat{\mathbf{u}} \times \boldsymbol{\Omega}_0) \right] - 4\varepsilon M \nabla^2 (\nabla \cdot \hat{\mathbf{u}}) / 3 + O(\bar{\varepsilon}) \end{aligned} \quad (15)$$

The second is the vorticity-driven response given by

$$\begin{aligned} \nabla \cdot \tilde{\mathbf{u}} + O(\bar{\varepsilon}) = & 0, \\ \tilde{\mathbf{u}}_t = & -M \left[\nabla (\tilde{\mathbf{u}} \cdot \mathbf{u}_0) - \tilde{\mathbf{u}} \times \boldsymbol{\Omega}_0 - \mathbf{u}_0 \times \tilde{\boldsymbol{\Omega}} \right] - \varepsilon M \nabla \times \tilde{\boldsymbol{\Omega}} + O(\bar{\varepsilon}) \end{aligned} \quad (16)$$

Since $\varepsilon M < M$, $\forall \varepsilon < 1$, damping due to viscosity can be ignored at $O(M)$ in Eq. (15). For longitudinal oscillations, the ensuing pressure and velocity can be written as

$$\begin{aligned} \hat{p}(x, t) = & \cos(\omega_m x) \exp(-i\omega_m t) + O(M), \\ \hat{\mathbf{u}}(x, t) = & i \sin(\omega_m x) \exp(-i\omega_m t) \mathbf{e}_x + O(M), \end{aligned} \quad (17)$$

where $\omega_m = \omega a / c = m\pi / l$, $m = 1, 2, 3, \dots$ for a tube that is acoustically closed at both ends. Solutions corresponding to the closed-open (nozzleless) tube can be obtained straightforwardly by replacing m by $(m - 1/2)$ everywhere. In much the same way, the oscillatory vortical response can be expressed by

$$\tilde{\mathbf{u}} = \bar{\mathbf{u}} \exp(-i\omega_m t), \quad \tilde{\boldsymbol{\Omega}} = \bar{\boldsymbol{\Omega}}(x, r) \exp(-i\omega_m t), \quad (18)$$

where $\bar{\mathbf{u}} \equiv \bar{u}_x \mathbf{e}_x + \bar{v}_r \mathbf{e}_r$, and $\bar{\boldsymbol{\Omega}} \equiv \nabla \times \bar{\mathbf{u}} = \bar{\Omega}_\theta \mathbf{e}_\theta$. Instead of Eq. (16), we now have

$$\begin{aligned} \nabla \cdot \bar{\mathbf{u}} + O(\bar{\varepsilon}) = & 0, \\ iS\bar{\mathbf{u}} = & \left[\nabla (\bar{\mathbf{u}} \cdot \mathbf{u}_0) - \bar{\mathbf{u}} \times \boldsymbol{\Omega}_0 - \mathbf{u}_0 \times \bar{\boldsymbol{\Omega}} \right] + \varepsilon \nabla \times \bar{\boldsymbol{\Omega}} + O(\bar{\varepsilon} M^{-1}) \end{aligned} \quad (19)$$

where $S = \omega a / V > 10$ is the Strouhal number.

Following Flandro²⁷ and Majdalani and Roh,³³ we now assume that $\bar{v} / \bar{u} = O(M)$. The axial component of (19) becomes

$$iS\bar{u} = (u_0 \bar{u})_x + v_0 \bar{u}_r - \varepsilon r^{-1} (r \bar{u}_r)_x. \quad (20)$$

E. Vorticity and Momentum Transport

One may proceed to solve either the vorticity or momentum transport equations. In the first case, one must start by taking the curl of Eq. (19) to obtain

$$\begin{aligned} \bar{\Omega}_r - (r^{-1} + iSv_0^{-1})\bar{\Omega} + u_0 v_0^{-1} \bar{\Omega}_x = & -\bar{u} v_0^{-1} (\Omega_0)_x \\ & + \varepsilon v_0^{-1} (\bar{\Omega}_{xx} + \bar{\Omega}_{rr} + r^{-1} \bar{\Omega}_r - r^{-2} \bar{\Omega}) \end{aligned} \quad (21)$$

In the second case, $\tilde{\mathbf{u}}$ may be derived directly from the momentum equation. To that end, one must first rearrange Eq. (20) into

$$x\bar{u}_x = (i r S / F' - 1)\bar{u} + (F / F')\bar{u}_r + \varepsilon r (\bar{u}_{rr} + r^{-1} \bar{u}_r) / F'. \quad (22)$$

Using $\bar{u}(x, r) = X(x)R(r)$ and $\bar{u}(x, 1) = -i \sin(\omega_m x)$, one finds that Eq. (22) exhibits a solution of the form

$$\bar{u}(x, r) = -i \sum_{n=0}^{\infty} (-1)^n (\omega_m x)^{2n+1} R_n(r) / (2n+1)! \quad (23)$$

where R_n must be solved from

$$\begin{aligned} \varepsilon \frac{d^2 R_n}{dr^2} + r^{-1} (\varepsilon + F) \frac{dR_n}{dr} + [iS - (2n+2)r^{-1}F'] R_n = & 0, \\ & 0 \leq r \leq 1, \end{aligned} \quad (24)$$

with $R_n(1) = 1$ (no-slip), and $R_n'(0) = 0$ (25)

By virtue of Eq. (3), Eq. (24) admits a regular singularity at the core where $F(0) = 0$. In what follows, both WKB and two-variable multiple-scale expansions will be used to overcome this singularity.

Before initiating the asymptotic work, we introduce u_1^N as the numerical solution of the linearized momentum equation. It follows that u_1^N can be determined by coupling the numerical solution of Eq. (24) with Eqs. (23), (18), and (17).

III. The Vorticity Transport Technique

A. Vorticity Transport Equation

In this section, (21) will be used to derive asymptotic expressions for the rotational vorticity and velocity fields. When $\bar{\Omega} = \varpi_0 + M\varpi_1 + O(M^2)$ is used in (21), the leading-order equation becomes

$$(\varpi_0)_r - (r^{-1} + iSv_0^{-1})\varpi_0 + u_0 v_0^{-1} (\varpi_0)_x = 0. \quad (26)$$

Assuming a solution of the form $\varpi_0 = R(r)X(x)$, one gets

$$\varpi_0(x, r) = r \exp(-i\Phi_0) \sum_{\lambda_n} c_n (xF)^{\lambda_n}, \quad \lambda_n > 0;$$

$$\Phi_0(r) = S \int_1^r \frac{x dx}{F(x)} = \begin{cases} \frac{1}{4} S \ln[r^2 / (2 - r^2)], & \text{small } R \\ \frac{1}{\pi} S \ln \tan(\frac{1}{4} \pi r^2), & \text{large } R \end{cases} \quad (27)$$

Note that c_n must be specified in a manner to satisfy the no-slip condition at the wall. This condition must be expressed in terms of vorticity. Recalling that $\Omega_1 = \tilde{\Omega}$, $v_1 = \tilde{v}$, $p_1 = \hat{p}$, and that $u_1(x, 1, t)$ must vanish to prevent slippage, the axial projection of Eq. (12) gives, at the wall

$$M \left[(\tilde{v} v_0)_x - \tilde{v} \Omega_0 - v_0 \tilde{\Omega} \right] + \hat{p}_x + \varepsilon M (\tilde{\Omega}_r + r^{-1} \tilde{\Omega}) = 0. \quad (28)$$

Rearranging, and using Eq. (17), one gets

$$\tilde{\Omega}(x, 1) = S \sin(m\pi x / l) - \varepsilon (\bar{\Omega}_r + \bar{\Omega}) + O(M). \quad (29)$$

B. Inviscid Solution

At the wall, Eq. (29) must be equated to Eq. (27) in order to specify the separation eigenvalues. Since $F(1) = 1$ from (3), one can write $\varpi_0(x, 1) \equiv S \sin(\omega_m x)$.

This will be true when $\lambda_n = 2n + 1$ and

$$c_n = S (-1)^n (\omega_m)^{2n+1} / (2n+1)! \quad (30)$$

Recalling that $\Psi = xF$, backward substitution into Eq. (27) yields $\varpi_0(x, r) = rS \sin(\omega_m \Psi) \exp(-i\Phi_0)$.

Introducing $\bar{u} = r^{-1}\psi_r$ and $\bar{v} = -r^{-1}\psi_x$, the vorticity equation becomes

$$r\bar{\Omega} = -\psi_{xx} + r^{-1}\psi_r - \psi_{rr}. \quad (31)$$

When $\psi_0(x, r) = \psi_c(r)\varpi_0(x, r)$ is used in Eq. (31), a balance between leading-order quantities yields

$$\psi_c = r\Phi_0'^{-2} = S^{-2}r^{-1}F^2. \quad (32)$$

Differentiating the streamfunction for the velocity gives, at length,

$$\bar{\mathbf{u}}(x, r) = -F[\mathbf{i}\sin(\omega_m\Psi)\mathbf{e}_x + Mr^{-1}F^2\cos(\omega_m\Psi)\mathbf{e}_r]\exp(-\mathbf{i}\Phi_0). \quad (33)$$

C. Viscous Corrections

In order to properly account for viscous effects, we set

$$\begin{aligned} \bar{\mathbf{u}}(x, r) &= u_c(r)\sin(\omega_m\Psi)\exp(-\mathbf{i}\Phi_0) \text{ and,} \\ \bar{\Omega}(x, r) &= \varpi_c(r)\sin(\omega_m\Psi)\exp(-\mathbf{i}\Phi_0) \end{aligned} \quad (34)$$

The viscous correction multipliers, u_c and ϖ_c , are then found in a manner to satisfy the complete vorticity transport equation. In fact, when Eq. (34) is substituted into Eq. (21), one notes the cancellation of several terms. Balancing the remaining quantities requires that

$$d\varpi_c/dr - (\varepsilon S^2 r^3 F^{-3} + r^{-1})\varpi_c + (F'' - F'r^{-1})F^{-1}u_c = 0 \quad (35)$$

At this point, a relation between u_c and ϖ_c is needed to make any headway. Defining $\xi \equiv \varepsilon S^2 = a\nu\omega^2 V^{-3}$, we realize that $10^{-2} < \xi < 10^2$, $10^{-1} < \varepsilon^{1/2}S < 10$, $S = O(\varepsilon^{-1/2})$, and $S \sim \sqrt{R}$. Next we use (20) and find that $u_c = -S^{-1}(\mathbf{i}Fr^{-1} + \xi S^{-1}rF^{-1})\varpi_c$. Inserting this expression into Eq. (35) leads to

$$\begin{aligned} d\varpi_c/dr - [\xi r^3 F^{-3} + r^{-1} + \mathbf{i}S^{-1}r^{-1}(F'' - r^{-1}F')] \varpi_c &= 0, \\ \varpi_c(r) &= Cr \exp \zeta_0 \end{aligned} \quad (36)$$

where

$$\begin{aligned} \frac{\zeta_0}{\xi} &= \int_1^r x^3 F^{-3}(x) dx \\ &= \begin{cases} -\frac{1}{32} \left[3 \ln(2r^{-2} - 1) + 2(1 - r^{-2}) \right] \\ \times (2r^4 - 3r^2 - 4)(2 - r^2)^{-2}, & \text{small } R \\ -\pi^{-2} \left[\csc \theta + \theta \cot \theta \csc \theta \right] \\ -1 - I(\theta) + I\left(\frac{1}{2}\pi\right); & \theta \equiv \frac{\pi}{2}r^2, \text{ large } R \end{cases} \end{aligned} \quad (37)$$

$$I(x) = x + \sum_{k=1}^{\infty} (-1)^k 2(1 - 2^{2k-1}) B_{2k} x^{2k+1} / (2k+1)! \quad (38)$$

The integration constant C in Eq. (36) can be specified from Eq. (29). Noting that $\zeta_0'(1) = \xi$, $\Phi_0'(1) = S$, and $\zeta_0(1) = \Phi_0(1) = 0$, we find $C(1 - \mathbf{i}\varepsilon S) = S + O(S^{-2})$. Hence,

$$C^r = S / (1 + \varepsilon^2 S^2), \text{ and } C^i = \varepsilon S^2 / (1 + \varepsilon^2 S^2). \quad (39)$$

Straightforward substitution into Eqs. (36), (34), and (18) yields $\bar{\Omega} = Cr \sin(\omega_m\Psi)\exp(\zeta_0 - \mathbf{i}\Phi_0 - \mathbf{i}\omega_m t)$. The corrective multiplier is therefore

$$u_c = -S^{-1}(\mathbf{i}r^{-1}F + \varepsilon S r F^{-1}) Cr \exp \zeta_0 \equiv \mathbf{i}Ur \exp \zeta_0 \quad (40)$$

where

$$U^r = -S^{-1}C^r r^{-1}F - \varepsilon C^i r F^{-1}, \quad U^i = \varepsilon C^r r F^{-1} - S^{-1}C^i r^{-1}F, \quad (41)$$

Next, \tilde{u} may be obtained from Eqs. (34) and (18). The outcome is $\tilde{u} = \mathbf{i}rU \sin(\omega_m\Psi)\exp(\zeta_0 - \mathbf{i}\Phi_0 - \mathbf{i}\omega_m t)$. Having fully determined \tilde{u} , \tilde{v} can be obtained, at leading order, from mass conservation. Starting with $\tilde{v} = r^{-1}g(r)\cos(\omega_m\Psi)\exp(\zeta_0 - \mathbf{i}\Phi_0 - \mathbf{i}\omega_m t)$, substitution into $r^{-1}(r\tilde{v})_r + \tilde{u}_x = 0$ requires that $g = MrUF^2$. Using the superscript ‘V’ for the vorticity transport formulation, key results obtained heretofore can be summarized in

$$\begin{aligned} u_1^V &= \sin(\omega_m x) \sin(\omega_m t) \\ -r(U^r \sin \varphi - U^i \cos \varphi) \exp \zeta_0 \sin(\omega_m x F), \quad \varphi &= \omega_m t + \Phi_0 \end{aligned} \quad (42)$$

$$v_1^V = MF^2(U^r \cos \varphi + U^i \sin \varphi) \exp \zeta_0 \cos(\omega_m x F), \quad (43)$$

$$\Omega_1^V = (C^r \cos \varphi + C^i \sin \varphi) r \exp \zeta_0 \sin(\omega_m x F). \quad (44)$$

IV. The WKB Technique

A. The WKB Expansion

Formal WKB theory³⁹ suggests setting

$$R_n(r) = \exp(\delta^{-1}S_0 + S_1 + \delta S_2 + \delta^2 S_3 + \delta^3 S_4 + \dots), \quad (45)$$

where δ is a small parameter and $S_j(r)$ must be determined sequentially for $j \geq 0$. Straightforward differentiation and substitution into Eq. (24) yields the distinguished limit $\delta = \sqrt{\varepsilon}$ and $S\sqrt{\varepsilon} = O(1)$. The equation for S_0 becomes

$$Fr^{-1}S_0' + \mathbf{i}S\sqrt{\varepsilon} = 0, \quad S_0(1) = 0 \quad (46)$$

or

$$S_0(r) = -\mathbf{i}S\sqrt{\varepsilon} \int_1^r x F^{-1}(x) dx = -\mathbf{i}\sqrt{\varepsilon}\Phi_0. \quad (47)$$

By the same token, one finds

$$Fr^{-1}S_1' + S_0'' - (2n+2)F'r^{-1} = 0, \quad S_1(1) = 0 \quad (48)$$

$$S_1(r) = (2n+2)\ln F + \xi \int_1^r x^3 F^{-3}(x) dx. \quad (49)$$

$$Fr^{-1}S_2' + S_0''' + 2S_0'S_1' + r^{-1}S_0' = 0, \quad S_2(1) = 0 \quad (50)$$

and so

$$\begin{aligned} S_2(r) &= \mathbf{i}S\sqrt{\varepsilon} \left\{ (2n + \frac{3}{2}) [1 - r^2 F^{-2}(r)] \right. \\ &\quad \left. + (4n + 5) \int_1^r x F^{-2} dx + 2\xi \int_1^r x^5 F^{-5} dx \right\} \end{aligned} \quad (51)$$

The first-order WKB solution can be constructed via Eq. (45). Using ‘W’ for WKB, one may write

$$R_n^W(r) = F^{2n+2} \exp(\zeta_0 - \mathbf{i}\Phi_0 - \mathbf{i}\Phi_1^n) + O(\varepsilon), \quad (52)$$

with

$$\Phi_1^n \equiv -\varepsilon S \left\{ (2n + \frac{3}{2}) [1 - r^2 F^{-2}(r)] + (4n + 5) \int_1^r x F^{-2} dx + 2\xi \int_1^r x^5 F^{-5} dx \right\} \quad (53)$$

For small and large R , Φ_1^n can be calculated from

$$\begin{aligned} \frac{\Phi_1^n}{\varepsilon S} &= \frac{1}{128} r^{-4} (2 - r^2)^{-4} \\ &\times \left[32\xi + 2r^2 \left\{ 16(2 - r^2)^2 (1 - r^2) \right. \right. \\ &\quad \left. \left. \times [16(1 + n) - (23 + 28n)r^2 + 2(3 + 4n)r^4] \right. \right. \\ &\quad \left. \left. + \xi \left\{ 48 + r^2 [6 - r^2(3 - r^2)(84 - 65r^2 + 16r^4)] \right\} \right\} \right] \\ &+ r^4 (2 - r^2)^4 (80 + 64n + 15\xi) \ln(2r^{-2} - 1) \end{aligned} \quad (54a)$$

for small R , and

$$\frac{\Phi_1^n}{\varepsilon S} = \pi^{-1} \left\{ (4n + 5) \cot \theta + (4n + 3) \left(\theta \csc^2 \theta - \frac{1}{2} \pi \right) \right. \\ \left. - 8\pi^{-2} \xi [T(\theta) - T(\frac{1}{2}\pi)] \right\} \quad (54b)$$

for large R . Here

$$\begin{aligned} T(x) &= \int x^2 \csc^5 x dx = \frac{1}{48} \left\{ 40 \ln \tan \frac{x}{2} + 9x^2 \right. \\ &\quad \left. - 2 \csc x [18x + (2 + 9x^2) \cot x] - 4x \csc^3 x (2 + 3x \cot x) \right\} \\ &\quad + \frac{3}{4} \sum_{k=1}^{\infty} (-1)^k (1 - 2^{2k-1}) B_{2k} x^{2k+2} / [(2k+2)(2k)!]. \end{aligned} \quad (55)$$

B. The First-order WKB Solution

Equation (52) can be inserted back into Eq. (23) to render

$$\begin{aligned} \bar{u}(x, r) &= -iF \exp(\zeta_0 - i\Phi_0 - i\Phi_1^n) \sum_{n=0}^{\infty} \frac{(-1)^n (\omega_m x F)^{2n+1}}{(2n+1)!} \\ &= -iF \exp(\zeta_0 - i\Phi_0 - i\Phi_1^n) \sin(\omega_m x F) \end{aligned} \quad (56)$$

This expression can be used in conjunction with Eqs. (18), (17), and (14) to construct the oscillatory velocity component. At length, one finds

$$\begin{aligned} u_1^W(x, r, t) &= \sin(\omega_m x) \sin(\omega_m t) \\ &\quad - F \sin(\omega_m x F) \exp \zeta^W \sin(\omega_m t + \Phi^W) \end{aligned} \quad (57)$$

$$\zeta^W = \zeta_0, \Phi^W = \Phi_0 + \Phi_1^0,$$

$$\Phi_1^0 = -\varepsilon S \left\{ \frac{3}{2} [1 - r^2 F^{-2}(r)] + 5 \int_1^r x F^{-2} dx + 2\xi \int_1^r x^5 F^{-5} dx \right\} \quad (58)$$

wherein

$$\begin{aligned} \Phi_1^0 &= \frac{1}{128} \varepsilon S \left[r^4 (2 - r^2)^4 (80 + 15\xi) \ln(2r^{-2} - 1) \right. \\ &\quad \left. + 2r^2 \left(16(2 - r^2)^2 (1 - r^2) (16 - 23r^2 + 6r^4) \right. \right. \\ &\quad \left. \left. + \xi \left\{ 48 + r^2 [6 - r^2(3 - r^2)(84 - 65r^2 + 16r^4)] \right\} \right\] + 32\xi \right] \\ &\quad \times r^{-4} (2 - r^2)^{-4}, \quad \text{small } R \end{aligned} \quad (59a)$$

or

$$\Phi_1^0 = \pi^{-1} \varepsilon S \left\{ 5 \cot \theta + 3 \left(\theta \csc^2 \theta - \frac{1}{2} \pi \right) \right. \\ \left. - 8\pi^{-2} \xi [T(\theta) - T(\frac{1}{2}\pi)] \right\}, \quad \text{large } R \quad (59b)$$

V. The Undetermined-Scale Technique

A. Nonlinear Transformation

A two-variable expansion requires specifying two fictitious coordinates, an outer scale r_0 , and an inner scale, r_1 . Conventional scaling transformations include variable selections of the form $r_1 = f(\varepsilon)r$, or $r_1 = f(\varepsilon)(1 - r)$. According to formal practices, the strict definition of $f(\varepsilon)$ must precede the expansion. The difficulty, in our case, is that conventional selections fail to yield uniformly valid solutions. In fact, we find it necessary to introduce a nonlinear variable transformation of the form $r_1 = \varepsilon s(r)$. Our choice is different in that $s(r)$ is not pre-set by foreknowledge, rationalization, or an order of magnitude analysis. Rather, it is left to be an undetermined function that can accommodate generally nonlinear distortions. This choice provides more freedom and enables us to determine $s(r)$ in a manner to satisfy the problem's solvability condition. The latter can be rigorously prescribed using either Prandtl's principle of matching by supplementary expansions, or the principle of least singular behavior.

B. The Two-Scale Expansion

Introducing $r_0 = r$ and $r_1 = \varepsilon s(r)$, functions and derivatives can be expanded in a manner to discard $O(\varepsilon^2)$ quantities. Using superscripts to denote perturbation orders, one can assume the Poincaré expansion

$$\begin{aligned} R_n(r_0, r_1) &= R^{(0)}(r_0, r_1) + \varepsilon R^{(1)}(r_0, r_1) + O(\varepsilon^2), \\ \frac{d}{dr} &= \frac{\partial}{\partial r_0} + \varepsilon \frac{ds}{dr_0} \frac{\partial}{\partial r_1}, \quad \frac{d^2}{dr^2} = \frac{\partial^2}{\partial r_0^2} + O(\varepsilon). \end{aligned} \quad (60)$$

Inserting these expansions into Eq. (24), terms of the same power in ε can be collected. The result is

$$\begin{aligned} \frac{\partial R^{(0)}}{\partial r_0} + \left[i \frac{r_0 S}{F} - 2(n+1) \frac{F'}{F} \right] R^{(0)} &= 0; \\ R^{(0)}(1) = 1, \quad \frac{\partial R^{(0)}}{\partial r_0}(0) &= 0. \end{aligned} \quad (61)$$

$$\begin{aligned} \frac{\partial R^{(1)}}{\partial r_0} + \left[i \frac{r_0 S}{F} - 2(n+1) \frac{F'}{F} \right] R^{(1)} &= \\ = -\frac{ds}{dr_0} \frac{\partial R^{(0)}}{\partial r_1} - \frac{1}{F} \frac{\partial R^{(0)}}{\partial r_0} - \frac{r_0}{F} \frac{\partial^2 R^{(0)}}{\partial r_0^2} \end{aligned} \quad (62)$$

Since $F(1) = 1$ is a property of all Berman functions, integration of the leading-order equation yields

$$R^{(0)}(r_0, r_1) = a_1(r_1) \exp \left[2(n+1) \ln F(r_0) - iS \int_1^{r_0} x F^{-1}(x) dx \right]. \quad (63)$$

Here, a_1 must be determined in a manner to ensure a secular-free series expansion of R_n . This can be

achieved when the right-hand side of Eq. (62) is set to zero. The resulting first-order differential equation in a_1 can be integrated in closed form (using $\eta(1) = 0$, $R_n(1) = 1$, and $s(1) = 0$). Expressed in the original laboratory coordinate, one obtains

$$a_1 = \exp\left(-\xi\eta r^3 F^{-3} \left\{1 - 2S^{-2} (n+1)r^{-2} \left[F(F'' + r^{-1}F') + (2n+1)F'^2\right] + iS^{-1}r^{-2} [rF'(4n+3) + 2F]\right\}\right) \quad (64)$$

The effective scale functional $\eta(r)$ that appears in (64) is

$$\eta(r) \equiv -s(r)/s'(r). \quad (65)$$

Knowing $\eta(r)$, the rest is straightforward substitution into Eq. (63). Recalling that the overall solution is sought at $O(\bar{\varepsilon}M^{-1})$, retention of $R^{(0)}$ is sufficient. Subsequently, Eq. (60) becomes

$$R_n = F^{2n+2} \exp\left(-\xi\eta r^3 F^{-3} - iS \left\{\int_1^r xF^{-1}dx + \xi S^{-2}r\eta F^{-3} [rF'(4n+3) + 2F]\right\} + O(\varepsilon)\right) \quad (66)$$

C. Prandtl's Principle of Matching by Supplementary Expansions

Based on Prandtl's principle of matching by supplementary functions, the undetermined-scale solution developed here must exhibit the same leading-order terms obtained using the basic WKB expansion. Physically, the spatial damping function in Eq. (66) must match its counterpart arising in the WKB solution. This will be the case when

$$\eta^U(r) = -r^{-3} F^3(r) \int_1^r x^3 F^{-3}(x) dx \quad (67)$$

As usual, the superscript 'U' is used to denote the result based on the undetermined-scale technique. Having determined η^U , the undetermined coordinate transformation can be specified from Eq. (65). The result is

$$s^U(r) \sim \int_1^r x^3 F^{-3}(x) dx = \begin{cases} \left\{ \frac{1}{32} r^3 (2-r^2)^3 \left[\frac{\ln \frac{(2-r^2)^3}{r^6}}{r^6} + 4 + \frac{2[4+3r^2(r^2-3)]}{r^2(2-r^2)^2} \right] \right\}, & \text{small } R \\ \pi^{-2} \left[\csc \theta + \theta \cot \theta \csc \theta - 1 \right] r^{-3} \sin^3 \theta, & \text{large } R \end{cases} \quad (68)$$

Equation (68) is a key expression that unravels the dependence of $s(r)$ on the Berman function F . The algebraic content of Eq. (68) may be reason for the futility of standard multiple-scale methods.

D. The Undetermined-Scale Solution

Having determined R_n , Eq. (66) can be substituted into Eqs. (23) and (18), and then added to Eq. (17). One gets

$$u_1(x, r, t) = -iF \sum_{n=0}^{\infty} \frac{(-1)^n (\omega_m x F)^{2n+1}}{(2n+1)!} \exp(-\xi\eta r^3 F^{-3} - iS \times \left\{ \int_1^r xF^{-1}dx + \xi S^{-2}r\eta F^{-3} [rF'(4n+3) + 2F] \right\} - i\omega_m t) + i \sin(\omega_m x) \exp(-i\omega_m t) + O(\varepsilon). \quad (69)$$

Since the error associated with $n \geq 1$ terms is smaller than the error at $n = 0$, corrections of $O(S^{-2})$ can be retained for $n = 0$ and dismissed for $n \geq 1$. The equivalent expression for u_1 is

$$u_1 = i \exp(-i\omega_m t) \left(\sin(\omega_m x) - F \sin(\omega_m x F) \right) \times \exp\left\{-\xi\eta r^3 F^{-3} - iS \left[\int_1^r xF^{-1}dx + \varepsilon r \eta F^{-3} (3rF' + 2F) \right]\right\} \quad (70)$$

The meaningful part of the solution is identical to Eq. (57), namely,

$$u_1^U(x, r, t) = \sin(\omega_m x) \sin(\omega_m t) - F \sin(\omega_m x F) \exp \zeta^U \sin(\omega_m t + \Phi^U) \quad (71)$$

where

$$\zeta^U = \zeta_0 = -\xi\eta^U r^3 F^{-3}, \Phi^U = \Phi_0 + \Phi_1 = S \left[\int_1^r xF^{-1}dx + \varepsilon r \eta^U F^{-3} (3rF' + 2F) \right]. \quad (72)$$

E. Total Solution

From the axial component \tilde{u} , the radial velocity \tilde{v} can be obtained by appealing to continuity. To expedite the process, one may let

$$\tilde{v}(x, r, t) = r^{-1} G(r) \cos(\omega_m x F) \exp \zeta \exp[-i(\omega_m t + \Phi)] \quad (73)$$

where $G(r)$ is a subsidiary function that must be determined so that $\tilde{u}_x + r^{-1}(r\tilde{v})_r = 0$. After some algebra, we find that $G = -MF^3$. By differentiating \tilde{u} and \tilde{v} , the temporal vorticity is also obtainable. The total periodic components become

$$v_1^U(x, r, t) = -Mr^{-1} F^3 \cos(\omega_m x F) \exp \zeta^U \cos(\omega_m t + \Phi^U) \quad (74)$$

$$\Omega_1^U = rS \sin(\omega_m x F) \exp \zeta^U \cos(\omega_m t + \Phi^U). \quad (75)$$

Despite their dissimilar expressions, both v_1^U and Ω_1^U agree, almost to a fault, with Eq. (43).

VI. The Generalized-Scale Technique

A. Nonlinear Transformation

In the previous section, the modified variable is left unspecified while carrying out the two-scale expansion. At the conclusion of the asymptotic analysis, physical arguments are employed to evaluate the required transformation. These physical arguments are based on comparisons with the basic WKB solution. Despite the novelty in retaining an undetermined scale throughout the derivation process, the main limitation plaguing the previous approach lies in its strict dependence on the availability of an alternative approximation. This limitation is caused by Prandtl's principle requiring the

presence of at least one other expansion for the same problem.

The main purpose of this section is to present a different approach that leads to the independent specification of the inner scaling transformation. This will be obtained by imposing the problem's solvability condition stemming from the principle of minimum singularity. At the outset, the generally nonlinear scale will be determined by satisfying the mathematical constraint requiring boundedness between successive asymptotic orders. Unlike the former solutions, the current procedure precludes guessing and reveals, totally independently, the problem's intrinsic scales.

B. The Generalized Two-Scale Expansion

As before, we assume the Poincaré expansion

$$R_n(r_0, r_1) = R^{(0)}(r_0, r_1) + \varepsilon R^{(1)}(r_0, r_1) + O(\varepsilon^2) \quad (76)$$

where $r_0 = r$ and $r_1 = \varepsilon s(r)$. The only difference here is that the general transformation will have to originate from the problem's solvability condition. The leading-order solution can be readily put in the form

$$R^{(0)}(r_0, r_1) = C_1(r_1) \exp\left[2(n+1)\ln F(r_0) - iS \int_1^{r_0} xF^{-1}(x)dx\right] \quad (77)$$

where C_1 awaits evaluation from the first-order equation. This corrective multiplier must be determined in a manner to promote the least singular behavior in R_n . To that end, we find it unnecessary to determine $R^{(1)}$ fully. In fact, it will be sufficient to formulate a solvability condition for which an asymptotic series of the form $R^{(0)} + \varepsilon R^{(1)} + o(\varepsilon)$ can exist. This may be accomplished by first introducing

$$\Pi = \frac{R^{(1)}(r_0, r_1)}{R^{(0)}(r_0, r_1)}. \quad (78)$$

In order to determine Π , one can multiply Eq. (61) by $R^{(1)}[R^{(0)}]^{-2}$ and subtract the result from the product of Eq. (62) and $[R^{(0)}]^{-1}$. One gets

$$\begin{aligned} & \frac{1}{R^{(0)}} \frac{\partial R^{(1)}}{\partial r_0} - \frac{R^{(1)}}{[R^{(0)}]^2} \frac{\partial R^{(0)}}{\partial r_0} \\ &= -\frac{s'}{R^{(0)}} \frac{\partial R^{(0)}}{\partial r_1} - \frac{1}{FR^{(0)}} \frac{\partial R^{(0)}}{\partial r_0} - \frac{r_0}{FR^{(0)}} \frac{\partial^2 R^{(0)}}{\partial r_0^2} \end{aligned} \quad (79)$$

Noting that the left-hand-side is the derivative of Π , Eq. (79) can be written as

$$\begin{aligned} \frac{\partial \Pi}{\partial r_0} &= \frac{\partial}{\partial r_0} \left[\frac{R^{(1)}}{R^{(0)}} \right] = -\frac{s'}{C_1} \frac{dC_1}{dr_1} + S^2 r_0^3 F^{-3} - 2(n+1)F'F^{-2} \\ &\quad - 2(n+1)r_0 F''F^{-2} - 2(n+1)(2n+1)r_0^2 F'^2 F^{-3} \\ &\quad + iS r_0 F^{-2} + i(4n+3)S r_0^2 F'F^{-3}. \end{aligned} \quad (80)$$

Therefore,

$$\begin{aligned} \Pi &= -\frac{s}{C_1} \frac{dC_1}{dr_1} + S^2 \int_1^{r_0} \{x^3 F^{-3} - 2(n+1)S^{-2} \\ &\quad \times [F'F^{-2} + xF''F^{-2} + (2n+1)xF'^2 F^{-3}]\} dx. \end{aligned} \quad (81)$$

$$+iS^{-1}xF^{-2}[1+(4n+3)xF'F^{-1}]\} dx. \quad (81)$$

C. The Problem's Solvability Condition

In order to promote a uniformly valid asymptotic series, the ratio of $R^{(1)}$ and $R^{(0)}$ must be bounded $\forall r_1$. This can be accomplished by imposing $\Pi = O(1)$. For arbitrary F , Π will be bounded $\forall r_1$ if

$$\begin{aligned} & \frac{1}{C_1(r_1)} \frac{dC_1(r_1)}{dr_1} \equiv K(r_1) = O(1) \\ & \Rightarrow C_1 = C_0 \exp\left(\int K dr_1\right) = C_0 \exp\left(\varepsilon \int K ds\right). \end{aligned} \quad (82)$$

Here C_0 is a constant that can be later determined from $R^{(0)}(1) = 1$. Setting $K = \text{constant}$ will be sufficient (but not necessary) to guarantee boundedness. In fact, $K(r_1)$ will prove to be important for temporary bookkeeping. From Eq. (81), one finds

$$\begin{aligned} s &= K^{-1}S^2 \left(\int_1^{r_0} \{x^3 F^{-3} \right. \\ &\quad \left. - 2(n+1)S^{-2}F^{-2} [F' + xF'' + (2n+1)xF'^2 F^{-1}] \right. \\ &\quad \left. + iS^{-1}xF^{-2} [1 + (4n+3)xF'F^{-1}] \right\} dx - S^{-2}\Pi. \end{aligned} \quad (83)$$

Recalling that $\Pi = O(1)$, one can put

$$\begin{aligned} s &= K^{-1}S^2 \left(\int_1^{r_0} \{x^3 F^{-3} \right. \\ &\quad \left. + iS^{-1}xF^{-2} [1 + (4n+3)xF'F^{-1}] \right\} dx + O(S^{-2}). \end{aligned} \quad (84)$$

At this point, small corrections of $O(S^{-2} \sim \varepsilon)$ can be ignored. Partial differentiation of Eq. (84) gives

$$\partial s / \partial r_0 = K^{-1}S^2 \left\{ r_0^3 F^{-3} + iS^{-1}r_0 F^{-2} [1 + (4n+3)r_0 F'F^{-1}] \right\}. \quad (85)$$

When Eq. (85) is paired with Eq. (60), it can be seen that

$$\begin{aligned} ds &= (\partial s / \partial r_0 + \varepsilon s' \partial s / \partial r_1) dr = \\ & \left(K^{-1}S^2 \left\{ r_0^3 F^{-3} + iS^{-1}r_0 F^{-2} [1 + (4n+3)r_0 F'F^{-1}] \right\} + O(\varepsilon) \right) dr \end{aligned} \quad (86)$$

D. The Generalized-Scale Solution

In the process of substituting Eq. (86) back into Eq. (82), K is fully eliminated. One is left with

$$\begin{aligned} C_1 &= C_0 \cdot \\ & \times \exp\left(\varepsilon \int S^2 \left\{ r^3 F^{-3} + iS^{-1}r F^{-2} [1 + (4n+3)r F'F^{-1}] \right\} dr\right) \end{aligned} \quad (87)$$

Further substitution into Eq. (77) gives the leading-order solution

$$\begin{aligned} R_n &= F^{2n+2} \exp\left(\int_1^{r_0} \{\xi x^3 F^{-3} \right. \\ &\quad \left. - iS[xF^{-1} - \varepsilon xF^{-2} - (4n+3)\varepsilon x^2 F'F^{-3}]\} dx\right) \end{aligned} \quad (88)$$

where the boundary condition $R_n(1) = 1$ has been applied. Using $x^2 F' F^{-3} = (-\frac{1}{2} x F^{-2})' + x F^{-2}$, one simplifies Eq. (88) into

$$R_n^G = F^{2n+2} \exp \left[\int_1^{r_0} \left\{ \xi x^3 F^{-3} - i S [x F^{-1} - 4(n+1)\varepsilon x F^{-2}] \right\} dx + i(2n + \frac{3}{2})\varepsilon S(1 - r^2 F^{-2}) \right] + O(\varepsilon). \quad (89)$$

In the above, ‘G’ denotes a multiple-scale solution based on a generalized coordinate. The current solution can be expressed in the same form given by Eq. (71) and Eq. (75). The difference here is that Φ^G must be replaced by

$$\Phi^G = S \left[\int_1^r (x F^{-1} - 4\varepsilon x F^{-2}) dx + \frac{3}{2}\varepsilon (r^2 F^{-2} - 1) \right]; \quad (90)$$

$$\Phi^G = \begin{cases} -\frac{1}{4} S \left[(1-2\varepsilon) \ln(2r^{-2} - 1) + 2\varepsilon(1-r^{-2}) \right] \times (7-11r^2+3r^4)(2-r^2)^{-2}, & \text{small} \\ S\pi^{-1} \left[\ln \tan(\frac{1}{2}\theta) + \varepsilon \left[4 \cot \theta + 3(\theta \csc^2 \theta - \frac{1}{2}\pi) \right] \right], & \text{large } R \end{cases} \quad (91)$$

E. The General Characteristic Length

In the current analysis, determination of η is not a prerequisite for finding $s(r)$. Specification of the generalized scale in Eq. (84) is done exclusively by observing the principle of minimum singularity. From (84), the need for a nonlinear coordinate transformation is explicitly ascertained. Although unnecessary, the problem’s characteristic length scale can be evaluated from Eqs. (65), (84), and (86). One finds

$$\eta^G(r) \sim \frac{\int_1^r x^3 F^{-3} \left\{ 1 + i S^{-1} x^{-3} [x F + (4n+3)x^2 F'] \right\} dx}{-r^3 F^{-3} \left\{ 1 + i S^{-1} r^{-3} [r F + (4n+3)r^2 F'] \right\}} \quad (92)$$

which confirms that

$$s^G(r) \sim \int_1^r \left\{ x^3 F^{-3} + i S^{-1} x F^{-2} [1 + (4n+3)x F' F^{-1}] \right\} dx. \quad (93)$$

It is interesting to note that η^U can be restored from η^G since $\eta^G \rightarrow \eta^U$ as $S \rightarrow \infty$, $\forall n$. Thus η^U in Eq. (67) represents the dominant, leading-order part of η^G . Similarly, s^U in Eq. (68) is recoverable from s^G . This may explain the ability of the undetermined-scale technique to yield a uniformly valid approximation.

VII. Other Approximations

A. The Composite-Scale Technique

In two previous studies, Majdalani and Van Moorhem^{29,34} used a different approach to analyze the large injection problem. Following space-reductive multiple-scale theory, inner, outer, and intermediate scales were first identified and then replaced by one ‘composite’ function, $s^C(r) = (1-r)r^{-a(1-r)^b}$, with

$a = b = \frac{3}{2}$. The composite scale s^C was uniformly valid over the solution domain and could reproduce asymptotically the scales that existed near $r = 0, 1$. The corresponding η could be derived by direct differentiation of s^C . The resulting functional, namely,

$$\eta^C(r) = (1-r) \left\{ 1 + a(1-r)^b [(1-r)r^{-1} - b \ln r] \right\}^{-1} \quad (94)$$

was corroborated by Majdalani³² in a separate study covering the porous channel flow. For small injection, one finds $a = \frac{4}{3}$, and $b = \frac{8}{3}$. The composite-scale solution can now be reproduced by simply substituting η^C into Eqs. (71)–(72).

B. Zhao’s Approximation

In similar but independent work concerned with large sidewall injection in a tube, Zhao *et al.*³¹ introduced a nonlinear transformation also. However, Zhao’s transformation was based on the choice of two scales that were found by intuition. While the first scale was taken to be the radial distance from the wall, the second was based on a ‘much shorter length associated with the radial distance traveled by a fluid particle on the acoustic timescale.’ Subject to a minor correction in the lower bound of Zhao’s defining integral (i.e., the lower bound should be ‘1’ instead of ‘0’ lest the nonlinear scale be indeterminate), the two scales introduced by Zhao are

$$r_1 = 1 - r \equiv y, \text{ and } r_2 = M^{-1} V^{-1}(x) \int_1^{r_1} z \csc(\frac{1}{2}\pi z^2) dz. \quad (95)$$

Here $V(x)$ represents the normalized radial velocity distribution along the porous walls. For uniform injection, $V(x) = 1$. The scaling transformation employed by Zhao *et al.*³¹ can be extended to a problem with arbitrary injection. For that purpose, one must have

$$r_1 = 1 - r,$$

$$r_2 = M^{-1} V^{-1}(x) \int_1^{r_1} \frac{z dz}{F(z)} = \begin{cases} \frac{1}{4} M^{-1} V^{-1}(x) \\ \times \ln[y^2/(2-y^2)], & \text{small } R \\ \pi^{-1} M^{-1} V^{-1}(x) \\ \times \ln \tan(\frac{1}{4}\pi y^2), & \text{large } R \end{cases} \quad (96)$$

Using ‘Z’ to denote the scale functional based on the idea presented by Zhao *et al.*,³¹ one finds

$$\eta^Z = y^{-1} F(y) \int_1^y \frac{z dz}{F(z)} = \begin{cases} \frac{1}{4} y(2-y^2) \\ \times \ln[y^2/(2-y^2)], & \text{small } R \\ \pi^{-1} y^{-1} \sin(\frac{1}{2}\pi y^2) \\ \times \ln \tan(\frac{1}{4}\pi y^2), & \text{large } R \end{cases} \quad (97)$$

At this point, Zhao’s approximation can be obtained by substituting η^Z into Eqs. (71)–(72).

VIII. Results and Discussion

A. Characteristic Length Scales

So far several nonlinear length scales have been presented. Physically η^G , η^U , η^C , and η^Z represent approximations to the characteristic length scale for radial convection and attenuation of rotational disturbances. The intrinsic nonlinearity of η can be attributed to the co-existence of three important mechanisms evolving simultaneously on vastly dissimilar dimensions. These are viscous diffusion, radial convection, and unsteady inertia. While viscous forces diffuse vorticity on the small Stokes length, $\sqrt{2\nu/\omega}$, radial convection of unsteady vorticity evolves on a spatially varying wavelength. By analogy to the channel flow analysis,³³ the dimensional wavelength for radial propagation of vorticity waves can be shown to be $2\pi VF/(\omega r)$.

On one hand, both η^G and η^U are systematically determined *a posteriori* without the need for guessing. While η^U obeys Prandtl's principle of matching by supplementary functions, η^G is derived from the coordinate transformation prescribed by the principle of minimum singularity. Due to the validity of both principles, it is not surprising that η^U can be recovered from η^G for large S . On the other hand, both η^C and η^Z are introduced at the beginning of the asymptotic analysis. While η^C requires repeated trials to identify

the inner scales, η^Z is obtained following a rough scaling analysis. Despite the different modes of analysis used in their determination, these scales exhibit interesting similarities. Figure 2 illustrates their behavior for both large and small injection. Graphically, η^U and η^C seem to exhibit the same algebraic content despite their completely dissimilar expressions. Despite matching the endpoints at $r = 0, 1$, the appreciating discrepancy between η^Z and the formal scales can be attributed to the dependence of η^Z on F instead of F^3 . This may also explain the reduced precision that can be associated with Zhao's approximation.

It should be noted that the idea of a nonlinear scale is not entirely novel. It has been reported by Van Dyke⁴⁰ that a nonlinear transformation had been first introduced by Munson.⁴¹ The relevant work involved the convection-diffusion equation appropriate to the study of the vortical layer on an inclined cone. In that problem, linear stretching was ineffective, and an inner coordinate of the form $r_i = r^\epsilon$ had to be devised. The main novelty in the current analysis lies, perhaps, in the manner by which the scales are derived, *a posteriori*, by appealing to fundamental principles.

B. Comparison to Numerical Simulations of the Linearized Momentum Equation

A sample comparison between different velocity formulations is given in Table 1 for parameters

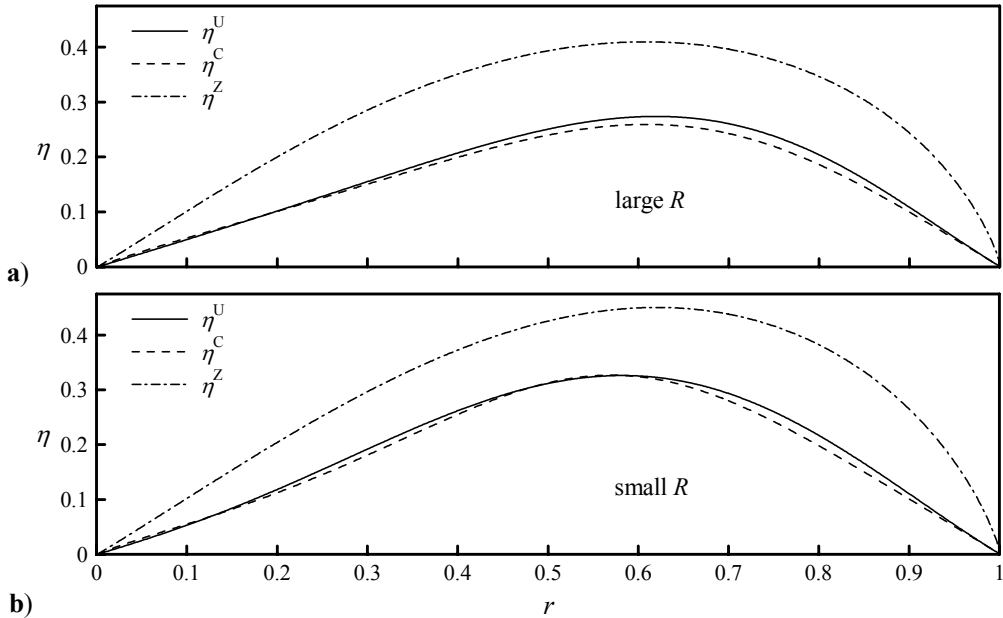


Fig. 2 Comparing the characteristic length scale η^U to existing theories for (a) large and (b) small crossflow Reynolds numbers. While η^C is the composite length scale derived by Majdalani and Van Moorhem,²⁹ η^Z is based on the scales introduced by Zhao *et al.*³¹

Table 1. Temporal velocity comparisons for a typical cold flow experiment with $S = 50m$, $\xi = (\frac{1}{2})m^2$, $R = 5000$, $\omega_m t = (\frac{1}{2})\pi$, $x/l = \frac{1}{2}$, and $m = 1$

r	u_1^N	u_1^W	u_1^G	u_1^U	u_1^C	u_1^V	u_1^Z
0.25	1.0046531	1.0044774	1.0039328	1.0043514	1.0044372	1.003676	1.0018561
0.30	1.0067035	1.0066087	1.0051425	1.006438	1.006511	1.004387	1.0044809
0.35	0.9733651	0.9737435	0.9724632	0.9737617	0.9731331	0.971751	0.9842647
0.40	0.9903954	0.9903039	0.9932655	0.9898707	0.9899531	0.995357	0.9892226
0.45	1.0744999	1.074372	1.0718149	1.0750839	1.0759036	1.069648	1.0635215
0.50	0.8573811	0.8575266	0.859535	0.8566916	0.855174	0.861564	0.8753034
0.55	1.2053590	1.205421	1.2032398	1.2066581	1.2085849	1.200635	1.1859822
0.60	0.7684439	0.7678885	0.7708428	0.7657254	0.7639084	0.775048	0.7827293
0.65	1.1456849	1.1469024	1.1433344	1.1501326	1.1507553	1.137126	1.1448204
0.70	1.1237301	1.1221856	1.1252955	1.1188044	1.1208156	1.132144	1.1043363
0.75	0.4871556	0.4881371	0.4866488	0.490051	0.4850715	0.482291	0.5255649
0.80	1.7483207	1.7485428	1.7484048	1.748745	1.7543405	1.747759	1.7052073
0.85	0.4647273	0.4637707	0.4643581	0.4626698	0.4599853	0.468972	0.4888941
0.90	0.9031535	0.9038142	0.9036781	0.9043345	0.9036394	0.899133	0.9145188
0.95	1.7406562	1.7405539	1.740445	1.740594	1.741614	1.742110	1.7055102

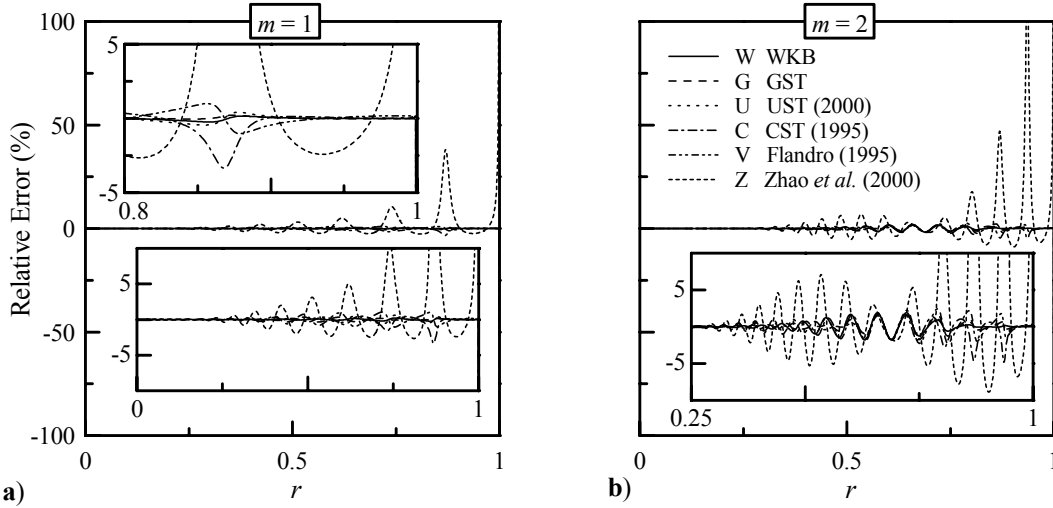


Fig. 3 Error entailed in the various asymptotic formulations for u_1^W , u_1^G , u_1^U , u_1^C , u_1^V , and u_1^Z . For the first two oscillation modes, we compare solutions for a typical cold-flow experiment with $S = 50m$ and $R = 5000$. Results are presented at acoustic pressure nodes corresponding to (a) $x/l = \frac{1}{2}$, and (b) $x/l = \frac{1}{3}$. Relative deviations from the numerical solution appear to be contained within $\pm 5\%$ at the exception of u_1^Z . Enlargements are shown in the insets.

corresponding to a typical cold-flow experiment. It is reassuring to note the overall concurrence of various asymptotic techniques and the numerical solution of the linearized Navier–Stokes equation. This good agreement actually persists over a broad range of physical parameters. Using u_1^N as a benchmark, relative errors are determined and plotted in Fig. 3 for the first two oscillation modes and the same physical setting. Whereas discrepancies between most asymptotic

solutions and u_1^N are almost too small to be discerned graphically, the error in u_1^Z exhibits large random peaks that reflect non-uniformity. These random deviations become more pronounced at higher oscillation modes. This result can be attributed to the clear differences (shown in Fig. 2) between η^U and Zhao’s assumed function η^Z .

C. Computational Verification

The most striking result is, perhaps, the good agreement found when asymptotic predictions are compared with numerical simulations of the complete set of (nonlinear) Navier–Stokes equations. Inasmuch as small nonlinearities are not incorporated in the analytical derivations, deviations between asymptotics and numerical simulations turn out to be smaller than expected. A sample comparison is provided in Fig. 4 for the first three oscillation modes of a typical large injection case. While the axial locations are chosen to coincide with harmonic pressure nodes, results obtained are based on the fully implicit, finite volume code developed by Roh, Tseng and Yang.³⁷ The small discrepancies between asymptotic and computational data are ascribed to the finite space and time discretization errors, and to small nonlinearities that elude the asymptotic model. Note, in particular, the presence of $j - 1$ rotational velocity nodes downstream of the j th internal velocity node in Figs. 4c, e and f. These nodes appear in the computational solution for $m > 1$ and concur with the forthcoming description.

D. Experimental Verification

In order to better understand the oscillatory flow character over transpiring surfaces, numerous velocity and pressure measurements have been gathered during cold-flow experiments conducted by Brown and co-workers.^{19,35} Their tests were carried out using a circular tube that allowed steady sidewall injection of Nitrogen gas. Their setup corresponded to: $S = 51.3m$, $R = 4900$, $M = 0.0018$, $L = 1.727m$, $a = 0.0508m$, $c = 290 \text{ m s}^{-1}$, $\nu = 5.43 \times 10^{-6} \text{ m}^2 \text{ s}^{-1}$, and $\omega = 168\pi m \text{ rad s}^{-1}$. Using three-element hot wire probes positioned in an upstream portion of the tube (where the flow is strongly laminar), experimental measurements were collected for the first two oscillation modes (84 and 168 Hz), and for two dimensionless pressure ratios by Brown *et al.*³⁵ While velocity amplitudes are shown in Figs. 5a–b for the first two oscillation modes, the velocity-to-pressure phase lags are compiled in Figs. 5c–d. Comparisons with asymptotic predictions show satisfactory agreement between theory and experiment. This agreement becomes more convincing when experimental acquisition and calibration errors are

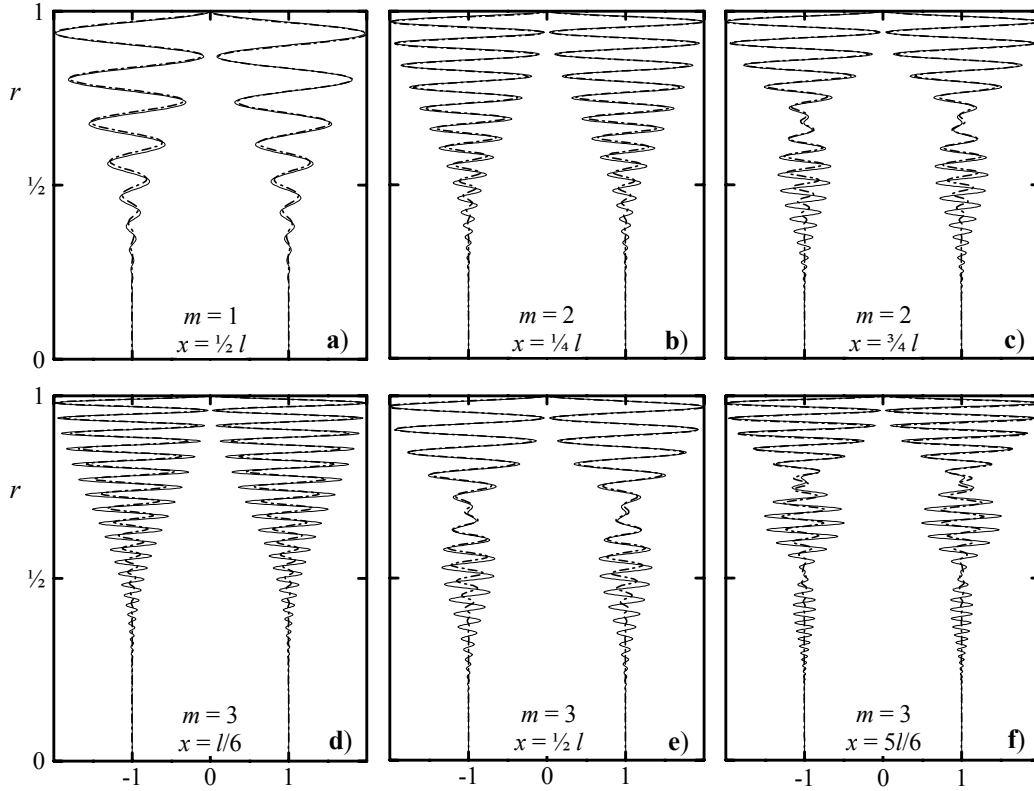


Fig. 4 Comparison at two successive times between our asymptotic solution for u_1 (full lines) and numeric simulations of the nonlinear Navier-Stokes equations (chains). For the first three oscillation modes, profiles are provided at axial positions corresponding to acoustic pressure nodes. Here $S = 50m$, $R = 4 \times 10^4$, and $\xi = m^2 / 16$. Discrepancies between numerics and asymptotics can be attributed, in part, to the finite mesh resolution of (a) 60×150 , (b-c) 80×240 , and (e-f) 90×360 (in the axial and radial directions) for $m = 1, 2$ and 3.

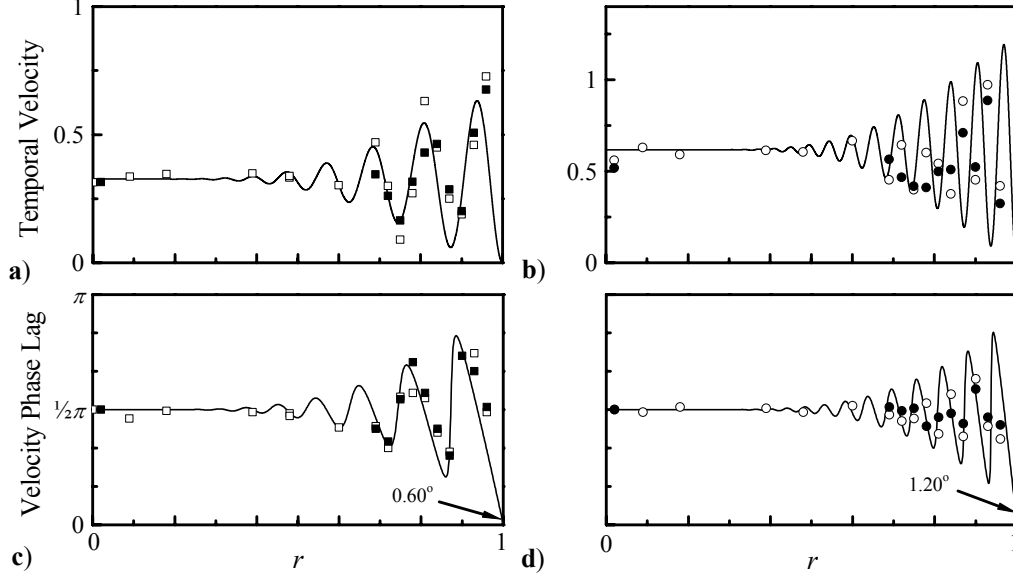


Fig. 5 Comparison between our asymptotic solution for u_1 (full lines) and experimental data obtained by Brown *et al.*³⁵ For $m = 1$ and 2 , temporal velocity amplitudes are shown in (a) and (b) while their phase angles (with respect to pressure) are shown in (c) and (d). Similarity parameters correspond to $S = 51.3m$, $R = 4900$, and $x/l = 0.106$. Other parameters are $M = 0.0018$, $l = 34$, $\omega_m = (\pi/34)m$, and $\xi = 0.539m^2$. Hollow and dark symbols correspond to experimental data acquired with a pressure wave amplitude $\bar{\varepsilon}$ of 0.0005 and 0.0039 . Squares and circles are used to denote first and second oscillation modes. With reference to Brown *et al.*,³⁵ our symbols (\square), (\circ), (\blacksquare), and (\bullet) are for tables VI, VII, VIII, and IX.

factored in. Note that, at the wall, the phase lag can be calculated, following Majdalani,³⁶ to be:

$$\pi/2 - \arctan(R/S). \quad (98)$$

This result can be numerically verified $\forall F$.

E. Evolution of Unsteady Velocity and Vorticity

Unlike the vorticity transport formulation, the generalized-scale solution is sufficiently compact to provide simple expressions for a number of flow features. Included are the depth of penetration, Richardson overshoot factor, phase lag, and velocity modulus. The first three features have been covered, for large R , by Majdalani.³⁶ The arbitrary injection case can be similarly treated. The velocity modulus will be now examined because of its usefulness in describing the flow character across the tube's finite length.

For a typical test case, $|u_1|$ can be evaluated and shown in Fig. 6 at several discrete locations. For the first three oscillation modes, patterns are clearly influenced by the inviscid pressure mode shapes. Rotational amplitudes are largest along the wall near harmonic pressure nodes where the pressure-driven velocity response is most intense. Pressure nodes may be identified by $x/l = (2j-1)/2m$, $1 \leq j \leq m$, for the j th internal pressure node. The additional downstream intensification of rotational amplitudes is due to the axial convection of unsteady vorticity by the mean

flow. Conversely, a weakening in vortical strength is noted during inward propagation. The vortical attenuation in the radial direction can be attributed to the compounding effects of viscous diffusion and the speed reduction in the convective motion. Irrespective of the acoustic oscillation mode, one observes, near the wall, an overshoot in the unsteady velocity amplitude. Commonly referred to as the Richardson annular effect,⁴² this phenomenon is more intense near the wall where the large vortical response can favorably couple with the pressure-driven response.

At higher oscillation modes ($m > 1$), the presence of premature nodes of zero rotational amplitude is noted $j < m$ times downstream of the j th internal velocity node. These irrotational points are caused by the lines of zero vorticity that originate at the velocity nodes ($x/l = j/m$) and stretch across the solution domain. In fact, when $|u_1|$ is plotted at several axial locations, the rotational nodes are found to appear at the radial intersections with the zero vorticity streaklines.

Whereas acoustic velocity nodes correspond to zero vorticity points, the most appreciable vorticity sources appear at the pressure nodes. In fact, a close examination of Eq. (29) confirms that fresh vorticity is constantly supplied at the wall where the oscillatory pressure gradient in the axial direction is perpendicular to the radially incoming flow. Thus $\bar{\Omega}(x,1)$ is highest at

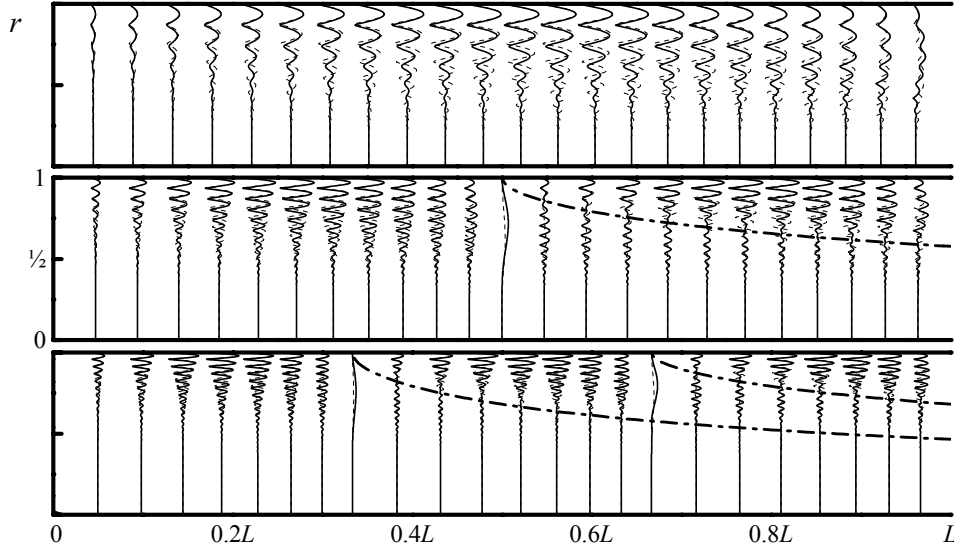


Fig. 6 From top to bottom, the modulus of unsteady velocity is plotted at several axial locations and for the first three oscillation modes. Results are shown for geometrically similar tubes (solid lines) and channels (broken lines). Physical parameters are $R = 4 \times 10^4$, $\xi = m^2/16$, and $S = 50m$. A pattern correlation with classic acoustic mode shapes is apparent. Maximum rotational amplitudes occur near acoustic pressure nodes and diminish in the direction of velocity nodes. Rotational amplitudes are not symmetric with respect to pressure nodes as they increase downstream due to the mean flow convection of unsteady vorticity. The presence of premature zero rotational amplitudes for $m = 2, 3$ are due to streaks of zero vorticity (chain lines) emanating from the j th internal velocity nodes located at $x/l = j/m$, $j < m$. The penetration of vorticity is more significant in a channel (broken lines).

$x/l = (2j-1)/2m$ where $\hat{p} = 0$ and \hat{u} exhibits the maximum amplitude given by Eq. (17). Since the total vorticity can be written as

$$\Omega = Mx(F'/r - F'')/r + \bar{\varepsilon}rS \sin[m\pi(x/l)F] \exp \zeta \cos(\omega_m t + \Phi) \quad (99)$$

it is clear that the maximum $\bar{\Omega}(x,1)$ is of order $\bar{\varepsilon}S/M = \omega_m \bar{\varepsilon}/M^2$ in comparison to the steady vorticity. Recalling from Eq. (13) that $\bar{\varepsilon}/M^2 > 1$, it follows that unsteady vorticity can be more intense than the mean flow vorticity. The role played by unsteady vorticity is hence very important and should not be discounted in this or similar low surface Mach number models.

F. Curvature Effects

In order to illustrate the principal differences between axisymmetric and planar motions, results in Fig. 6 are shown for two geometrically similar ducts, namely, for a tube (solid lines) and a channel (broken lines) that exhibit circular and rectangular cross-sections. We find the inward penetration of vorticity to be more significant in a channel due to the absence of curvature. A curvature appears to inhibit the penetration depth of vorticity by reducing the flow cross-section normal to

incoming streams. For the same reason, the unsteady velocity amplitude decays more rapidly in a tube.

With respect to mean vorticity generation and transport, two interesting features can be noted. The first regards vorticity amplitudes. By comparing the mean flow velocity and vorticity in Eq. (2) to that in a channel,³³ one finds, for any position x ,

$$\frac{u_0(r=1)}{u_0(y=0)} = \begin{cases} \frac{8}{3} & \Omega_0(r=0) \\ 2 & \Omega_0(y=1) \end{cases} = \begin{cases} \frac{8}{3}, & \text{small } R \\ 4, & \text{large } R \end{cases} \quad (100)$$

Hence, for large R , $\Omega_0 = \pi^2 x$ is four times larger near the wall in a tube than in a channel with $\Omega_0 = \frac{1}{4} \pi^2 x$. Reasons can be attributed to the larger axial velocity in the tube. The larger amplitudes are compounded by vortex augmentation caused by the radial compression of circular vortex rings. Such compression is not present in the less vortical channel having the same aspect ratio. As explained by Flandro²⁷ and Majdalani, Flandro and Roh,⁴³ vorticity can lead to an important destabilizing term in solid rocket motor combustion that needs to be accounted for lest predictions fall short of actual measurements. From that perspective, an enhanced vortical field in a tube is likely to promote a less stable acoustic environment.

The second feature regards the transverse penetration of mean vorticity. Since vorticity is carried by the mean flow, its penetration depth is found to be more significant in a channel where a more gradual flow turning occurs. As flow turning requires energy to be transferred from the axial acoustic field to the radially incoming fluid, the energy exchange happens more rapidly near the walls of a tube. Despite the smaller local vorticity in the channel, the infinite radius of curvature allows vorticity rings to tap deeper into the core. Conversely, since a finite curvature inhibits the inward propagation of vorticity, a broader inviscid core is realized in a tube.

G. Comparison to Sexl's Profile

Since the mean flow is solely induced by the influx at the walls, suppressing injection drastically alters our model. As we approach the limiting process of zero injection, walls become impermeable and pressure loses its mean component. The question that could be raised is: where should one stop? We find that, if V in our model is made comparable to the Stokes diffusion speed, $\sqrt{2\omega\nu}$, our results will mimic Sexl's exact solution for an oscillatory flow bounded by rigid walls. In that event, dynamic similarity parameters can be chosen such that $\xi = \lambda_s$, where $\lambda_s = a\sqrt{\omega/2\nu}$ is the Stokes number. Accordingly, we will have $R = 2^{1/6}a\sqrt{\omega/\nu}$ and $V = \sqrt{2\omega\nu}/\sqrt[3]{2}$. The wall injection velocity will hence be slightly smaller than the diffusion speed. One may interpret this condition to be

reflective of insignificant injection. The resulting field can be compared to the exact solution given by Sexl⁴⁴ for an oscillating fluid inside an impermeable tube. The latter is derived for an infinitely long tube and exhibits first mode oscillations that are independent of x . Due to our tube's finite length, we compare u_1 in Fig. 7 to the exact solution at $x/l = 1/2$ and $m = 1$. Graphically, the comparison seems to indicate a favorable agreement between asymptotic and exact predictions. In particular, when injection is virtually absent, a reversal can be noted in the role played by viscosity. This phenomenon is consistent with Prandtl's classic theory foreseeing a deeper vortical presence at higher viscosity (Fig. 7a).

Overall, our approximate solution seems to embrace Sexl's solution when injection is reduced to the diffusion speed. Thus, although it is possible to approximate the one-dimensional oscillatory solution from ours, the converse is not true. Since $2^{1/6} \cong 1.12$, one may set the lower limit on the crossflow Reynolds number to be $R = a\sqrt{\omega/\nu} = 10$, so that $\varepsilon \leq 0.1$. This lower limit is prescribed, in part, by the desired precision in the ensuing perturbation analysis. At the lower end of the spectrum, properties must therefore satisfy $a\sqrt{\omega/\nu} > 10$ and $Va/\nu > 10$. The corresponding model remains applicable as long as

$$V > 10\nu/a \text{ and } \omega > 10V/a. \quad (101)$$

These inequalities set the lower bounds for an open-ended range of physical parameter encompassing many realistic flows.

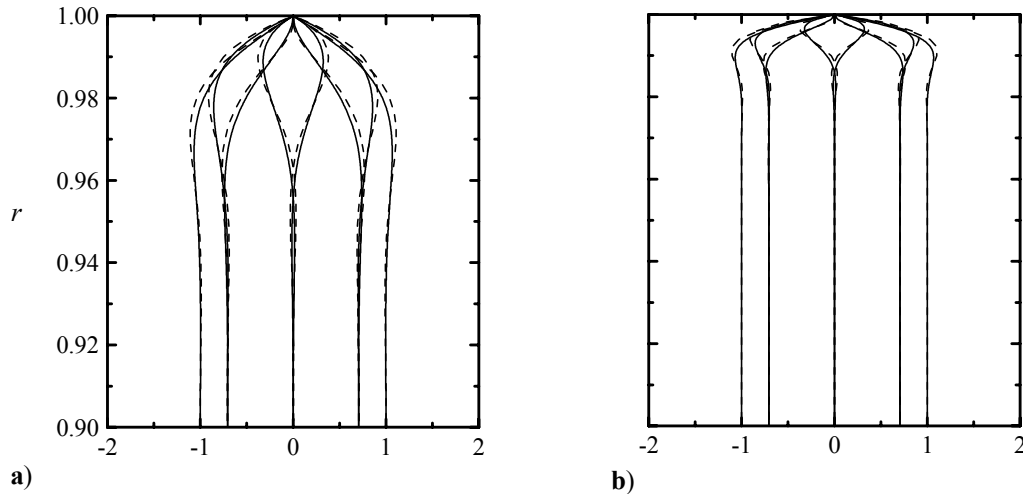


Fig. 7 Velocity profiles of u_1 shown at eight successive time intervals. Results are obtained from asymptotic predictions (broken lines) and the exact formula by Sexl (full lines). Parameters correspond to $\xi = \lambda_s$ for which convective and diffusive speeds are of the same order. We use $a\sqrt{\omega/\nu} = 100$ in (a) and $100\sqrt{10}$ in (b). In the absence of appreciable wall injection, the penetration of vorticity diminishes when viscosity is reduced—going from (a) to (b).

H. Viscosity and the Boundary Layer

Observations made in the channel analogue regarding the role of viscosity are reconfirmed here for an arbitrary mean flow function. For moderate-to-large injection speeds, the penetration depth is found to diminish with increasing viscosity. However, for sufficiently small injection, the depth of penetration decreases when viscosity is made smaller. In order to understand the seemingly paradoxical role played by viscosity, one needs to examine the details of the penetration depth, Δ^* . To begin, one needs to realize that Δ^* encompasses two adjacent regions: a highly vortical layer immediately above the wall followed by a highly viscous layer of $O(\sqrt{\nu/V})$ that is blown-off by the incoming stream.

For sufficiently small injection, the solution is a strongly damped wave whose viscous layer is formed in the close proximity of the wall. Moreover, it is much larger than the vortical layer pressed beneath it. The resulting depth of penetration becomes slightly larger than the Stokes layer of $O(\sqrt{\nu/\omega})$. Now when viscosity is increased, the viscous layer grows in size and the rate at which vorticity diffuses increases also. The enhanced diffusion rate causes the underlying vorticity layer to narrow in thickness. Since the vortical thickness is of order $V^3/(\omega^2\nu)$, it can be near zero for sufficiently small V ; as such, the net reduction in the vorticity sheet constitutes an insignificant contribution to the overall depth of penetration. The net growth in the viscous layer outweighs the net reduction in the thin vorticity layer to the point that a larger Δ^* is realized.

For appreciable injection reported in cold-flow studies, the highly viscous layer of $O(\sqrt{\nu/V})$ is now

pushed to the central portion of the tube.⁴⁵ It is much thinner than the vorticity layer of $O(a)$ (since $V^3/(\omega^2\nu) = a/\xi$ and $\xi \sim 1$). When viscosity is increased, the expansion of the thin viscous layer of $O(\nu^{1/2})$ becomes negligible in comparison to the contraction of $O(\nu^{-1})$ experienced by the vorticity layer. The ensuing Δ^* decreases when ν is made larger. In a sense, it is the relative sizes of vorticity and viscosity layers at different injection speeds that stand behind the dual roles played by viscosity.

I. Error Verification

Using u_1^N as a benchmark, the asymptotic error associated with u_1^W , u_1^G , u_1^U , u_1^C , and u_1^V can be evaluated. Following Bosley,⁴⁶ we define E_m to be the maximum absolute error between u_1^N and u_1 given asymptotically. Assuming a logarithmic variation of the form $E_m \propto \varepsilon^\alpha$, the slope α can be read from the log-log plot of E_m versus ε . This, of course, gives the order of the error. As we show in Fig. 8, $\alpha \rightarrow 1$ asymptotically in all cases. Pursuant to Bosley's arguments, the clear asymptotic behavior indicates that all asymptotic solutions are correct, uniformly valid, and exhibit errors of $O(\varepsilon)$ over a wide range of parameters. The errors associated with u_1^W and u_1^G remain, however, the smallest. The improved accuracy of u_1^W is offset by the increased algebraic complexity in evaluating its first-order correction terms (e.g., Eq. (59a)). The simplicity, accuracy, and ease of evaluating u_1^G make it our favorite solution.

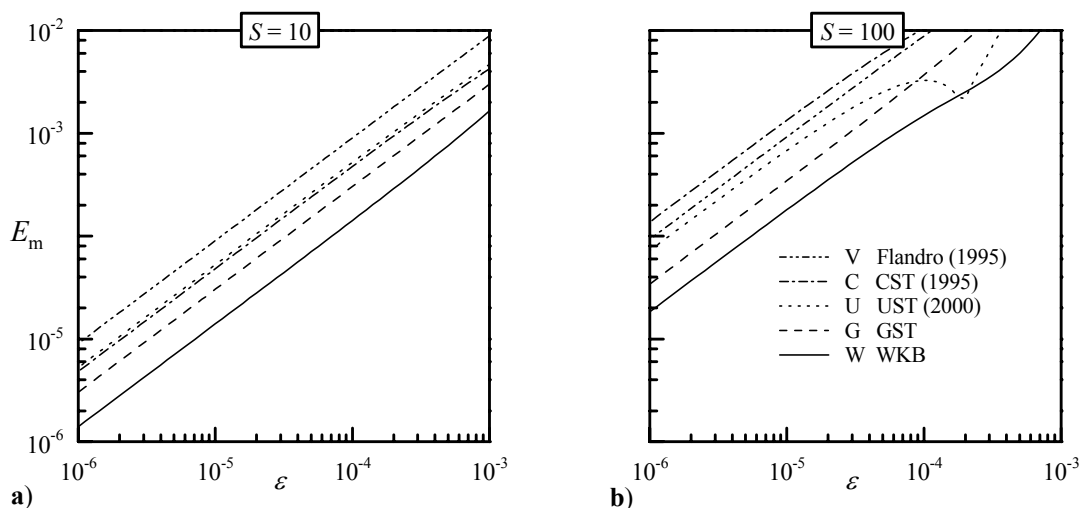


Fig. 8 Comparison of maximum errors entailed in u_1^W , u_1^G , u_1^U , u_1^C , and u_1^V for the large injection case. As $\varepsilon = R^{-1}$ is varied, the Strouhal number is held at (a) 10 and (b) 100. For every Strouhal number, the lowest curve that is indicative of the most accurate solution corresponds to u_1^W .

IX. Concluding Remarks

The quest for exact or asymptotic solutions of the viscous flow equations in porous tubes has a long history. In this work, we have presented a comprehensive account of the forms of asymptotic approximations that can proceed from the linearized vorticity and momentum transport equations. In contrast to previous studies of this topic that have addressed specific physical settings, we have implemented a systematic investigation using a general form of the mean flow field. Other authors have typically considered one level of injection in a given geometric setting. This work has demonstrated the possibility of presenting the final solution in a generic form that provides realizable expressions for any sufficiently differentiable mean flow function F . The generalized formulations show how not only do we recover (e.g., u_1^U and u_1^V), confirm (u_1^C), or correct previously attempted solutions (u_1^Z), but also find some completely new asymptotic forms (u_1^G and u_1^W). These have been catalogued in their most simple forms in Secs. III to VII. Any of them can be repeated for a more elaborate setting that includes, for example, the effects of expanding or contracting walls, nonuniformly permeable boundaries, and suction instead of injection. They can also be used to study the onset of hydrodynamic instability in the tube. As such, they open new lines of further inquiry.

Our solutions are especially useful in correcting deficiencies in current predictive algorithms used to determine the system stability in solid rocket motors. By demonstrating that unsteady vorticity exceeds in magnitude its steady counterpart, we have established the importance of implementing the elements of vorticity, viscosity, and other flow interactions not incorporated previously. To avoid combustion instabilities late in the development cycle, corrective procedures that include vorticity effects, such as those developed here, must therefore be accommodated in the analysis of oscillatory flows in high energy propulsion systems and industrial burners.

From a physical standpoint, our formulations promote a complete flow characterization that displays interesting vorticity and velocity patterns. These patterns are strongly influenced by the acoustic pressure mode shapes. For example, we find the most significant sources of unsteady vorticity to be concentrated near pressure nodes (at $x/l = (2j-1)/2m$, $1 \leq j \leq m$). By comparing tube and channel flows, our study brings into focus the effect of a tube's radius of curvature. In comparison to a channel, a tube is found to exhibit faster flow turning near the wall. It also induces magnifications in core velocities and vorticities by $(\frac{8}{3}, \frac{8}{3})$ and $(2, 4)$ for small and large R . While a smaller

radius of curvature inhibits the inward penetration of mean and unsteady vorticity, it promotes larger vortical magnitudes.

It is reassuring that our mathematical models, which have been hypothetical in nature, could be corroborated by experimental and computational tests. It is also vital that our formulations could reproduce exact solutions (such as Sexl's) and confirm, correct, or recover previously reported approximations. In the case of the generalized-scale technique, the ensuing work encompasses a completely new and rigorous method of analysis. The underlying multiple-scale structure encountered here can be attributed to the co-evolution of radial convection and viscous diffusion of vorticity waves on separate radial dimensions. Similar interactions can be present in other convection-diffusion problems that have been, heretofore, impossible to solve.

References

- ¹Taylor, G. I., "Fluid Flow in Regions Bounded by Porous Surfaces," *Proceedings of the Royal Society, London, Series A*, Vol. 234, No. 1199, 1956, pp. 456-475.
- ²Goto, M., and Uchida, S., "Unsteady Flows in a Semi-Infinite Expanding Pipe with Injection through Wall," *Transactions of the Japan Society for Aeronautical and Space Sciences*, Vol. 33, No. 9, 1990, pp. 14-27.
- ³Culick, F. E. C., "Rotational Axisymmetric Mean Flow and Damping of Acoustic Waves in a Solid Propellant Rocket," *AIAA Journal*, Vol. 4, No. 8, 1966, pp. 1462-1464.
- ⁴Berman, A. S., "Laminar Flow in Channels with Porous Walls," *Journal of Applied Physics*, Vol. 24, No. 9, 1953, pp. 1232-1235.
- ⁵Yuan, S. W., and Finkelstein, A. B., "Laminar Pipe Flow with Injection and Suction through a Porous Wall," *Transactions of the American Society of Mechanical Engineers: Journal of Applied Mechanics, Series E*, Vol. 78, No. 3, 1956, pp. 719-724.
- ⁶Terrill, R. M., and Thomas, P. W., "On Laminar Flow through a Uniformly Porous Pipe," *Applied Scientific Research*, Vol. 21, 1969, pp. 37-67.
- ⁷Durlofsky, L., and Brady, J. F., "The Spatial Stability of a Class of Similarity Solutions," *The Physics of Fluids*, Vol. 27, No. 5, 1984, pp. 1068-1076.
- ⁸Terrill, R. M., "On Some Exponentially Small Terms Arising in Flow through a Porous Pipe," *Quarterly Journal of Mechanics and Applied Mathematics*, Vol. 26, No. 3, 1973, pp. 347-354.
- ⁹Skalak, F. M., and Wang, C.-Y., "On the Nonunique Solutions of Laminar Flow through a Porous Tube or Channel," *SIAM Journal on Applied Mathematics*, Vol. 34, No. 3, 1978, pp. 535-544.
- ¹⁰Lu, C., "On the Existence of Multiple Solutions of a Boundary Value Problem Arising from Laminar Flow through a Porous Pipe," *Canadian Applied Mathematics Quarterly*, Vol. 2, No. 3, 1994, pp. 361-393.
- ¹¹Brady, J. F., and Acrivos, A., "Steady Flow in a Channel or Tube with an Accelerating Surface Velocity. An Exact Solution to the Navier-Stokes Equations with Reverse Flow," *Journal of Fluid Mechanics*, Vol. 112, 1981, pp. 127-150.

- ¹²Brady, J. F., "Flow Development in a Porous Channel or Tube," *The Physics of Fluids*, Vol. 27, No. 5, 1984, pp. 1061-1067.
- ¹³Gol'dshtik, M. A., and Ersh, N. M., "Stability of Pipe Flow with Blowing," *Fluid Dynamics (Izvestiya Akademii Nauk SSSR, Mechanika Zhidkosti i Gaza)*, Vol. 24, No. 1, 1989, pp. 51-59.
- ¹⁴Wageman, W. E., and Guevara, F. A., "Fluid Flow through a Porous Channel," *The Physics of Fluids*, Vol. 3, No. 6, 1960, pp. 878-881.
- ¹⁵Yuan, S. W., and Brogren, E. W., "Turbulent Flow in a Circular Pipe with Porous Walls," *The Physics of Fluids*, Vol. 4, No. 3, 1961, pp. 368-372.
- ¹⁶Olson, R. M., and Eckert, E. R. G., "Experimental Studies of Turbulent Flow in a Porous Circular Tube with Uniform Fluid Injection through the Tube Wall," *Transactions of the American Society of Mechanical Engineers: Journal of Applied Mechanics, Series E*, Vol. 33, 1966, pp. 7-17.
- ¹⁷Sviridenkov, A. A., and Yagodkin, V. I., "Flow in the Initial Sections of Channels with Permeable Walls," *Fluid Dynamics (Izvestiya Akademii Nauk SSSR, Mechanika Zhidkosti i Gaza)*, Vol. 11, No. 5, 1976, pp. 689-693.
- ¹⁸Beddini, R. A., "Injection-Induced Flows in Porous-Walled Ducts," *AIAA Journal*, Vol. 24, No. 11, 1986, pp. 1766-1773.
- ¹⁹Dunlap, R., Blackner, A. M., Waugh, R. C., Brown, R. S., and Willoughby, P. G., "Internal Flow Field Studies in a Simulated Cylindrical Port Rocket Chamber," *Journal of Propulsion and Power*, Vol. 6, No. 6, 1990, pp. 690-704.
- ²⁰Ma, Y., Van Moorhem, W. K., and Shorthill, R. W., "Innovative Method of Investigating the Role of Turbulence in the Velocity Coupling Phenomenon," *Journal of Vibration and Acoustics-Transactions of the ASME*, Vol. 112, No. 4, 1990, pp. 550-555.
- ²¹Ma, Y., Van Moorhem, W. K., and Shorthill, R. W., "Experimental Investigation of Velocity Coupling in Combustion Instability," *Journal of Propulsion and Power*, Vol. 7, No. 5, 1991, pp. 692-699.
- ²²Barron, J., Majdalani, J., and Van Moorhem, W. K., "A Novel Investigation of the Oscillatory Field over a Transpiring Surface," *Journal of Sound and Vibration*, Vol. 235, No. 2, 2000, pp. 281-297.
- ²³Griffond, J., and Casalis, G., "On the Nonparallel Stability of the Injection Induced Two-Dimensional Taylor Flow," *The Physics of Fluids*, Vol. 13, No. 6, 2001, pp. 1635-1644.
- ²⁴Casalis, G., Avalon, G., and Pineau, J.-P., "Spatial Instability of Planar Channel Flow with Fluid Injection through Porous Walls," *The Physics of Fluids*, Vol. 10, No. 10, 1998, pp. 2558-2568.
- ²⁵Flandro, G. A., "Solid Propellant Acoustic Admittance Corrections," *Journal of Sound and Vibration*, Vol. 36, No. 3, 1974, pp. 297-312.
- ²⁶Flandro, G. A., "Effects of Vorticity Transport on Axial Acoustic Waves in a Solid Propellant Rocket Chamber," *Combustion Instabilities Driven by Thermo-Chemical Acoustic Sources, NCA Vol. 4*, American Society of Mechanical Engineers, New York, 1989, pp. 53-61.
- ²⁷Flandro, G. A., "Effects of Vorticity on Rocket Combustion Stability," *Journal of Propulsion and Power*, Vol. 11, No. 4, 1995, pp. 607-625.
- ²⁸Flandro, G. A., "On Flow Turning," AIAA Paper 95-2530, July, 1995.
- ²⁹Majdalani, J., and Van Moorhem, W. K., "The Unsteady Boundary Layer in Solid Rocket Motors," AIAA Paper 95-2731, July 10-12, 1995.
- ³⁰Majdalani, J., and Van Moorhem, W. K., "A Multiple-Scales Solution to the Acoustic Boundary Layer in Solid Rocket Motors," *Journal of Propulsion and Power*, Vol. 13, No. 2, 1997, pp. 186-193.
- ³¹Zhao, Q., "Nonlinear Acoustic Processes in Solid Rocket Engines," Ph.D. Dissertation, University of Colorado, 1994.
- ³²Majdalani, J., "A Hybrid Multiple Scale Procedure for Boundary Layers Involving Several Dissimilar Scales," *Journal of Applied Mathematics and Physics*, Vol. 49, No. 6, 1998, pp. 849-868.
- ³³Majdalani, J., and Roh, T. S., "The Oscillatory Channel Flow with Large Wall Injection," *Proceedings of the Royal Society, Series A*, Vol. 456, No. 1999, 2000, pp. 1625-1657.
- ³⁴Majdalani, J., and Van Moorhem, W. K., "Improved Time-Dependent Flowfield Solution for Solid Rocket Motors," *AIAA Journal*, Vol. 36, No. 2, 1998, pp. 241-248.
- ³⁵Brown, R. S., Blackner, A. M., Willoughby, P. G., and Dunlap, R., "Coupling between Velocity Oscillations and Solid Propellant Combustion," Final Technical Rept. F49620-81-C-0027, Bolling Air Force Base, Washington DC, August 1986.
- ³⁶Majdalani, J., "The Boundary Layer Structure in Cylindrical Rocket Motors," *AIAA Journal*, Vol. 37, No. 4, 1999, pp. 505-508.
- ³⁷Roh, T. S., Tseng, I. S., and Yang, V., "Effects of Acoustic Oscillations on Flame Dynamics of Homogeneous Propellants in Rocket Motors," *Journal of Propulsion and Power*, Vol. 11, No. 4, 1995, pp. 640-650.
- ³⁸Terrill, R. M., "Laminar Flow through a Porous Tube," *ASME Journal of Fluid Engineering*, Vol. 105, 1983, pp. 303-307.
- ³⁹Bender, C. M., and Orszag, S. A., *Advanced Mathematical Methods for Scientists and Engineers*, McGraw-Hill Book Company Inc., New York, 1978.
- ⁴⁰Van Dyke, M., *Perturbation Methods in Fluid Mechanics*, The Parabolic Press, Stanford, CA, 1975.
- ⁴¹Munson, A. G., "The Vortical Layer on an Inclined Cone," *Journal of Fluid Mechanics*, Vol. 20, No. 4, 1964, pp. 625-643.
- ⁴²Rott, N., "Theory of Time-Dependent Laminar Flows," *High Speed Aerodynamics and Jet Propulsion - Theory of Laminar Flows*, Section D, Vol. IV, edited by F. K. Moore, Princeton University Press, Princeton, New Jersey, 1964, pp. 395-438.
- ⁴³Majdalani, J., Flandro, G. A., and Roh, T. S., "Convergence of Two Flowfield Models Predicting a Destabilizing Agent in Rocket Combustion," *Journal of Propulsion and Power*, Vol. 16, No. 3, 2000, pp. 492-497.
- ⁴⁴Sextl, T., "Über Den Von E.G. Richardson Entdeckten 'Annulareffekt'," *Zeitschrift für Physik*, Vol. 61, 1930, pp. 349-362.
- ⁴⁵Proudman, I., "An Example of Steady Laminar Flow at Large Reynolds Number," *Journal of Fluid Mechanics*, Vol. 9, No. 4, 1960, pp. 593-612.
- ⁴⁶Bosley, D. L., "A Technique for the Numerical Verification of Asymptotic Expansions," *SIAM Review*, Vol. 38, No. 1, 1996, pp. 128-135.